Atmos. Chem. Phys. Discuss., 15, 28395–28452, 2015
www.atmos-chem-phys-discuss.net/15/28395/2015/
doi:10.5194/acpd-15-28395-2015
© Author(s) 2015. CC Attribution 3.0 License.

Atmospheric Chemistry and Physics Discussions

This discussion paper is/has been under review for the journal Atmospheric Chemistry and Physics (ACP). Please refer to the corresponding final paper in ACP if available.

Wind speed response of marine non-precipitating stratocumulus clouds over a diurnal cycle in cloud-system resolving simulations

J. Kazil[1,2], **G. Feingold**[2], **and T. Yamaguchi**[1,2]

[1]Cooperative Institute for Research in Environmental Sciences (CIRES), University of Colorado, Boulder, Colorado, USA
[2]Chemical Sciences Division, Earth System Research Laboratory, NOAA, Boulder, Colorado, USA

Received: 2 September 2015 – Accepted: 23 September 2015 – Published: 21 October 2015

Correspondence to: J. Kazil (jan.kazil@noaa.gov)

Published by Copernicus Publications on behalf of the European Geosciences Union.

The simulations presented cannot answer this question! Only the transient response is studied.

does not make sense; edit

specify LW or SW CRE. I think you mean SW.

Abstract

Observed and projected trends in large scale wind speed over the oceans prompt the question: how might marine stratocumulus clouds and their radiative properties respond to future changes in large scale wind speed? Wind speed drives the surface fluxes of sensible heat, moisture, and momentum, and thereby acts on cloud liquid water path (LWP) and cloud radiative properties. We present an investigation of the dynamical response of non-precipitating, overcast marine stratocumulus clouds to different wind speeds, all else equal. In cloud-system resolving simulations, we find that higher wind speed leads to ~~faster boundary layer growth and~~ stronger entrainment. The dynamical driver is enhanced buoyant production of turbulence kinetic energy (TKE) from latent heat release in cloud updrafts. LWP is enhanced during the night and in the morning at higher wind speed, and more strongly suppressed later in the day. Wind speed hence accentuates the diurnal LWP cycle by expanding the morning – afternoon contrast. The higher LWP at higher wind speed does not, however, enhance cloud top cooling because in clouds with LWP $\gtrapprox 50\,\mathrm{g\,m^{-2}}$, long wave emissions are ~~very~~ insensitive to LWP. This leads to the more general conclusion that in sufficiently thick stratocumulus clouds, additional boundary layer growth and entrainment due to a boundary layer moistening arises by stronger production of TKE from latent heat release in cloud updrafts, rather than from enhanced longwave cooling. We find furthermore that large scale wind modulates boundary layer decoupling. At nighttime and at low wind speed during daytime, it enhances decoupling in part by faster boundary layer growth and stronger entrainment, and in part because circulation driven by shear from large scale wind in the sub-cloud layer hinders vertical moisture transport between the surface and cloud base. With increasing wind speed, however, in decoupled daytime conditions, shear-driven circulation due to large scale wind takes over from buoyancy-driven circulation in transporting moisture from the surface to cloud base, and thereby reduces decoupling and helps maintain LWP. The cloud radiative effect (CRE) responds to changes in LWP and cloud fraction, and higher wind speed translates to a stronger

why?

?

LES

what?

??

diurnally averaged CRE. However, the sensitivity of the diurnally averaged CRE to wind speed decreases with increasing wind speed. clarify

1 Introduction

Clouds are a linchpin in Earth's climate system because of their impact on Earth's radiation budget (Hartmann and Doelling, 1991). Low clouds, and in particular marine boundary layer clouds exert stronger leverage over reflected solar radiation compared to other cloud types (Hartmann and Short, 1980; Hartmann et al., 1992). With their response to environmental conditions, clouds amplify (positive cloud feedback) or dampen (negative cloud feedback) the effects of climate forcing or internal climate variability (Schneider, 1972; Stephens, 2005). Cloud feedbacks are a major source of uncertainty in climate simulations (Webb et al., 2006; Williams and Tselioudis, 2007; Wyant et al., 2006). The uncertainty related to low clouds originates primarily from marine stratocumulus and trade wind cumulus clouds (Bony and Dufresne, 2005; Soden and Vecchi, 2011). Recent observational and model work provides evidence for a positive low-level cloud feedback (Clement et al., 2009), but the sign, magnitude, and mechanisms of the response and feedback of low clouds to climate change are far from understood. The subject has therefore garnered intensifying scrutiny with models that resolve processes in more detail than climate models.

there are more recent papers that could be cited.

Caldwell and Bretherton (2009) found, using a mixed layer model, that a warmer climate would be accompanied by a negative cloud feedback from stratocumulus clouds, caused by a cloud thickening due to weaker mean subsidence and a stronger inversion. Xu et al. (2010) used a large eddy simulation (LES) model to investigate the response of shallow cumulus and overcast stratocumulus clouds in an idealized climate change scenario, represented by a 2 K warmer sea surface temperature (SST). They identified a negative cloud feedback arising from the increase of cloud geometric thickness, liquid water path (LWP), cloud optical thickness, and inversion height with SST. Blossey et al. (2013) investigated marine low cloud sensitivity to idealized climate change (2 K

same comment

SST warming) in a LES intercomparison study. The study covered the well-mixed stratocumulus, decoupled stratocumulus, and shallow cumulus cloud regimes. Most of the models in the intercomparison produced a negative cloud feedback for the well-mixed stratocumulus cloud regime, and a neutral or positive cloud feedback for the decoupled stratocumulus and the shallow cumulus cloud regime. Bretherton et al. (2013) expanded the investigation by considering changes in temperature, free-tropospheric relative humidity, carbon dioxide (CO_2) concentration, subsidence strength, inversion stability, and wind speed. The setup of their study allowed an estimate of the cloud response to a World Climate Research Program Coupled Model Intercomparison Project (CMIP3, Meehl et al., 2007) multimodel mean forcing for a particular greenhouse gas emission scenario. For a CMIP3 $2 \times CO_2$ forcing, a positive short-wave cloud feedback resulted for the well-mixed stratocumulus, decoupled stratocumulus, and shallow cumulus cloud regime. Bretherton et al. (2013) concluded that this result, relative to that of Caldwell and Bretherton (2009) and Xu et al. (2010), arose from accounting for the radiative effect of the addional CO_2 in their simulations, and from different assumptions on subsidence in a warmer climate and on the advection of heat and moisture. Combined, the current understanding indicates a positive globally integrated low cloud feedback in the climate system, but which is a composite of local responses which depend on cloud state and environmental conditions. Understanding of the various mechanisms by which the cloud states respond to changes in environmental conditions that accompany climate change is needed to build a dependable foundation for the representation of low level clouds in climate simulations.

The current study cannot address this.

An understudied cloud-climate feedback mechanism is the response of boundary layer clouds to changes in large scale wind speed. Colón-Robles et al. (2006) observed that weak surface winds were associated with fewer activated cloud droplets in trade wind cumulus clouds, and concluded that higher cloud droplet concentrations are more likely under conditions of stronger low-level wind speeds, primarily because stronger low-level wind speeds are associated with more intense cloud base updrafts. Chen et al. (2011) investigated aerosol–cloud–precipitation interactions in marine stra-

tocumulus using LES. They concluded that under stronger wind speed, an enhanced surface moisture flux leads to a thickening of the cloud and stronger precipitation. Nuijens and Stevens (2012) investigated the equilibrium response of trade wind cumulus clouds to wind speed using LES. They found that at stronger winds, trade wind cumulus clouds are deeper but not more numerous nor more energetic. Nuijens and Stevens identified the reason as an opposite response of the surface sensible heat and moisture fluxes to an increase in wind speed, which approximately maintains surface production of turbulence kinetic energy and cloud base mass fluxes as wind speed increases.

In this work, we investigate the response of non-precipitating, overcast marine stratocumulus clouds (Wood, 2012) to different wind speeds, all else equal. The goal is to identify and explain the dynamical processes by which wind speed acts on the evolution of boundary layer growth, entrainment, decoupling, LWP, and cloud radiative effect in the course of a diurnal cycle. We also investigate the role of buoyancy- and shear-driven dynamics for boundary layer growth, entrainment, decoupling, and LWP at different wind speeds.

The investigation is motivated by observed trends towards higher wind speeds over the oceans. Young et al. (2011) identified, using satellite radar altimeter wave heights, a global increase in ocean surface wind speed in the period 1991–2008. Hande et al. (2012) found an increasing surface wind speed trend spanning nearly four decades in radiosonde data at a location in the Southern Ocean. Bertin et al. (2013) identified a significant increase in wave height (driven by wind speed) in the North Atlantic Ocean over the 20th century, and Servain et al. (2014) found an intensification of trade winds in the tropical Atlanic over the period 1964–2012 that accompanied an observed warming trend in sea surface temperature. These trends in large scale wind speed are not necessarily a consequence of climate change, but could arise from internal climate variability (Dobrynin et al., 2015). Additional motivation derives from projected changes in ocean wind speeds and wave heights in the course of the 21st century (McInnes et al., 2011; Hemer et al., 2013). Together with an associated cloud response, the observed and projected changes in large scale wind speed would constitute a cloud-

climate feedback mechanism with the potential to impact Earth's radiation budget, the formation of precipitation, and the effect of aerosol on clouds.

Here we conduct cloud-system resolving simulations with different large scale wind speeds. The observed wind speed during the Second Dynamics and Chemistry of Marine Stratocumulus field study Research Flight 1 (DYCOMS II RF01, Stevens et al., 2005) serves as a reference for a ±25 % faster and slower large scale wind speed, respectively. We chose this variation because the associated variation in 10 m wind speed averaged over a diurnal cycle in our simulations (−18/ + 21 %) is comparable to the peak values of the 1991–2008 change in ocean surface wind speed at the location of the north-east Pacific coastal stratocumulus deck (Young et al., 2011). The different wind speeds drive different surface fluxes of sensible heat, moisture, and momentum in the simulations. We focus on the dynamical rather than the microphysical response of the stratocumulus-topped boundary layer to changes in wind speed, and excluded the effect of wind speed on surface aerosol production and loss by setting these terms to zero. The simulations are initialized with boundary layer properties, cloud properties, and dynamics that are consistent with DYCOMS II RF01 observations. The simulations are hence a suitable framework for identifing and characterizing the mechanisms by which the stratocumulus-topped marine boundary layer responds to different wind speeds, all else equal. However, they do not represent a stratocumulus-topped marine boundary layer in a future climate at different wind speeds, which would require initial and boundary conditions that are consistent with the chosen climate and wind speeds.

A key mechanism of the wind speed response of stratocumulus clouds is an increase or decrease of the surface moisture flux at higher or lower wind speed, respectively. This mechanism modulates cloud LWP, and thereby the response of the cloud to changes in aerosol concentration, as well as the propensity of the cloud to precipitate. In this work we focus on the non-precipitating stratocumulus state with a low precipitation susceptibility to aerosol concentration. The results of the simulations and the analysis are specific for this cloud state and the chosen environmental conditions.

Only the transient response is studied.

the effects should be through surface fluxes and TKE.

How much?

But not to new equilibria.

They also do not in the present climate, because they are not run to new equilibria.

why?

A number of studies (e.g., Wang et al., 2008, 2012; Katzwinkel et al., 2012; Mellado et al., 2014) have investigated the effect of strong wind shear at the inversion on stratocumulus clouds. Such shear is often caused by a jump in large scale wind speed and direction across the inversion, and differs qualitatively and quantitatively from shear that arises from the interaction of a constant large scale wind speed with the surface and with the potential temperature gradient at the inversion. In this work, we only consider shear that is generated by a constant large scale wind speed.

The text is organized as follows: Sect. 2 introduces the model and describes the spin-up runs and simulations. The final state of the spin-up runs (initial state of simulations) is compared with observations. Results are analyzed and discussed in Sect. 3. Conclusions are given in Sect. 4. Appendix A presents the nudging techniques used in the spinup-runs to generate conditions in the initial state of the simulations that are consistent with observations, and in the simulations to maintain mean free tropospheric potential temperature and water vapor profiles. Appendix B derives the boundary layer total water budget equation, and Appendix C discusses the resolution dependence of the results.

2 Model and simulations

We use the Advanced Research WRF (ARW) model (Skamarock et al., 2008), which includes optional chemical and aerosol processes (WRF/Chem, Grell et al., 2005), with the modifications described in Kazil et al. (2011, 2014). Because we focus on the response of the stratocumulus-topped marine boundary to wind speed via the surface fluxes of sensible heat, moisture, and momentum, we disabled chemical reactions, sea spray aerosol emissions, and aerosol dry deposition. We decompose the total wind field into a residual component and a constant geostrophic component. The model was modified so that its dynamical core only operates on the residual wind field (Kazil et al., 2014). This is permitted because the Navier–Stokes equations are invariant under Galilean transformations. The simulation domain can hence be thought of

should be added in quadrature

domain size? grid sizes?

why so large?

might be better to smaller domain and smaller grid sizes. the grid sizes are about 3x larger than recommended for LES of Sc

as moving with the geostrophic wind over a stationary ocean surface, although the geographic location, which determines the Coriolis parameter and insolation, is held fixed. The residual wind field is nudged by Rayleigh damping towards 0 over a 250 m layer at the domain top. At the domain base, geostrophic wind acts on the residual wind field by the interaction of the total wind field with the surface: the surface fluxes of sensible heat, moisture, and horizontal momentum are calculated from the sum of the horizontal residual wind speed and the horizontal geostrophic wind speed at the lowest model level. The simulation domain is periodic in the horizontal dimensions, with a height of 1650 m; it is located at 122° W, 31.5° N. The sea surface temperature is set to 291.5 K, 1 K below the sea surface temperature used in Stevens et al. (2005). This value produced in the final state of the spin-up runs (initial state of the simulations) a surface sensible heat and moisture flux of 14 and 122 $\mathrm{W\,m^{-2}}$, respectively (Stevens et al., 2005, give values of 15 and 115 $\mathrm{W\,m^{-2}}$, respectively). We use a surface pressure of 1017 hPa and a surface large scale divergence $\delta = 3.75 \times 10^{-6}\ \mathrm{s^{-1}}$ (Stevens et al., 2005).

2.1 Spin-up runs

The list of the spin-up runs is given in Table 1. The runs are labeled with the letters (medium) and / (large), which denote the domain size of 30 and 60 km, respectiv The reference grid spacing is $\mathrm{d}x = \mathrm{d}y = 150\,\mathrm{m}$, $\mathrm{d}z \approx 15\,\mathrm{m}$, $\mathrm{d}t = 1.5\,\mathrm{s}$, where $\mathrm{d}x$ and $\mathrm{d}y$ are the horizontal grid constants, $\mathrm{d}z$ the vertical grid constant, and $\mathrm{d}t$ the time step. The spin-up run m_{fine} uses double resolution in each dimension ($\mathrm{d}x = \mathrm{d}y = 75\,\mathrm{m}$, $\mathrm{d}z \approx 7.5\,\mathrm{m}$, $\mathrm{d}t = 0.75\,\mathrm{s}$). The spin-up run $l_{1:5}$ uses a reduced aspect ratio of (1 : 5), which is obtained by doubling horizontal resolution ($\mathrm{d}x = \mathrm{d}y = 75\,\mathrm{m}$, $\mathrm{d}z \approx 15\,\mathrm{m}$, $\mathrm{d}t = 1.5\,\mathrm{s}$).

2.1.1 Initialization

We prescribe altitude (z) profiles of potential temperature $\theta(z)$ and total water content $q_{\mathrm{t}}(z)$ as specified for DYCOMS II RF01 by Stevens et al. (2005) to initialize the

spin-up runs. Cloud water q_c and rain water q_r are initialized with zero values in the spin-up runs, hence the initial q_t is apportioned to q_v. The spin-up runs use the reference geostrophic wind speed with a horizontal west-east component $U = 7\,\mathrm{m\,s^{-1}}$ and a horizontal south-north component $V = -5.5\,\mathrm{m\,s^{-1}}$. The spin-up runs commence on 11 July 2001 at 00:00:00 UT, shortly after sunset, and end at 04:00:00 UT. Nudging (Appendix A) maintains the mean potential temperature profiles and the aerosol number concentration of $300\,\mathrm{mg^{-1}}$ throughout the simulation domain, and the total water profile in the free troposphere. Sedimentation and collision-coalescence of cloud drops are disabled to prevent drizzle formation.

This will affect the entrainment rate.

2.1.2 Temporal evolution

Figure 1 shows the spin-up run time series. Resolution, aspect ratio, and domain size cause only small differences in boundary layer (BL) turbulence kinetic energy (TKE) between the spin-up runs (Fig. 1a). Liquid water path (LWP) does not depend on domain size in the considered domain size range, but on resolution and aspect ratio (Fig. 1b). We discuss in the following the effect of resolution and aspect ratio, in the considered ranges, on the total water flux due to mixing across the inversion, and by extension, on LWP. The BL total water budget can be written as (Appendix B)

$$\frac{\mathrm{d}Q(t)}{\mathrm{d}t} = F^q_{\mathrm{precipitation}} + F^q_{\mathrm{surface}} - F^q_{\mathrm{entrainment}} - F^q_{\mathrm{subsidence}} - F^q_{\mathrm{mixing}}. \quad (1)$$

Q is the boundary layer mean total water mass path (vertically integrated total water mass per horizontal area). $F^q_{\mathrm{precipitation}}$ is the surface water flux due to precipitation, F^q_{surface} is the surface moisture flux, $F^q_{\mathrm{entrainment}}$ the total water flux across the inversion due to changes in mean inversion height, $F^q_{\mathrm{subsidence}}$ the total water flux across the inversion due to subsidence, and F^q_{mixing} the total water flux across the inversion due resolved scale and sub-grid scale dynamics at the inversion, fluctuations in inversion height, and spurious mixing. The fluxes point up when positive, which, together

with the level at which they are located (surface vs. inversion) explains their signs in Eq. (1). Note that none of the water variables (q_v, q_c, q_r, q_t) are nudged in the boundary layer (Appendix A), so that no nudging tendency needs to be accounted for in Eq. (1). Furthermore, $F^q_{\mathrm{entrainment}}$ can be taken as zero because mean potential temperature is nudged towards its initial profile (Appendix A), so that the mean inversion height exhibits only extremely small changes after approximately 90 min (Fig. 1c). $F^q_{\mathrm{precipitation}}$ is zero because sedimentation and collision-coalescence of cloud drops are disabled in the spin-up period. Equation (1) can therefore be simplified and rearranged to

WHY? This would seem to mask the physical impacts of wind speed.

$$F^q_{\mathrm{mixing}} = F^q_{\mathrm{surface}} - F^q_{\mathrm{subsidence}} - \frac{\mathrm{d}Q(t)}{\mathrm{d}t}. \quad (2)$$

Figure 1d shows the F^q_{mixing} time series from the spin-up runs; in the calculation of F^q_{mixing}, $F^q_{\mathrm{subsidence}}$ was approximated with its vertical component. Domain size has no effect on F^q_{mixing} in the considered domain size range, but mixing depends on resolution and aspect ratio. Doubling resolution in all dimensions reduces F^q_{mixing} by $\approx 20\,\mathrm{W\,m^{-2}}$, while reducing the aspect ratio from 1 : 10 to 1 : 5 increases F^q_{mixing} by $\approx 15\,\mathrm{W\,m^{-2}}$ (Fig. 1d). The different F^q_{mixing} change the temporal evolution of LWP in the spin-up runs (Fig. 1b). Relative to the spin-up runs m and l, the spin-up run with doubled resolution in all dimensions (m_{fine}) exhibits a higher (and increasing) LWP because of lower mixing across the inversion (Fig. 1d). The spin-up run with a reduced aspect ratio ($l_{1:5}$) exhibits a lower (and decreasing) LWP because of higher mixing across the inversion (Fig. 1d). The causal attribution relies on the fact that the differences in resolution and aspect ratio between the runs m, m_{fine}, l, and $l_{1:5}$ do not change BL TKE (Fig. 1a) and perturb surface moisture fluxes much less (in the range $\approx 5\,\mathrm{W\,m^{-2}}$, Fig. 1f) than the total water flux across the inversion due to mixing (in the range of $\approx 35\,\mathrm{W\,m^{-2}}$, Fig. 1d). It is therefore the response of mixing across the inversion to resolution and aspect ratio that causes the different temporal evolution of LWP, rather than a response of

Matching observations is not critical for a sensitivity study like this one.

For that reason, this section could be greatly shortened, or moved to the appendixes.

OK

the surface moisture flux or of boundary layer dynamics. To summarize, higher resolution in all dimensions reduces mixing across the inversion and drying of the boundary layer. A lower aspect ratio enhances mixing across the inversion and drying of the boundary layer. These findings indicate counteracting effects of vertical and temporal resolution vs. horizontal resolution on mixing at the inversion. Consequently, a model-specific aspect ratio range exists within which resolution-dependent effects sufficiently compensate each other so that the model can produce results that are consistent with observations.

2.1.3 Final state (initial state of simulations)

Figure 2 compares the final state of the spin-up runs (initial state of the simulations) with observations from DYCOMS II RF01 (Stevens et al., 2005). Liquid water potential temperature in the spin-up runs closely reproduces the observations (Fig. 2a) owing to nudging at all heights (Appendix A) towards the DYCOMS II RF01 specification. Water variables (q_v, q_c, q_r, q_t) are not nudged in the boundary layer. Total water observations are reproduced by the spin-up runs *m* and *l* (Fig. 2b) with no domain size dependence. Resolution and aspect ratio have a small impact on total water in the BL (Sect. 2.1.2): a higher resolution in all dimensions reduces drying of the BL, and total water increases; a reduced aspect ratio enhances drying of the BL, and total water decreases.

Cloud water is reproduced in part by the spin-up runs *m* and *l* (Fig. 2c), and cloud base cloud water is underestimated. This underestimate may be a consequence of absence of drizzle in the spin-up runs, caused by disabled sedimentation and collision-coalescence. While domain size has no effect on cloud water, resolution and aspect ratio do: a higher resolution in all dimensions reduces drying of the BL, and cloud water increases; a reduced aspect ratio enhances drying of the BL, and cloud water decreases (Sect. 2.1.2). The reduced aspect ratio spin-up run $l_{1:5}$ misses the observations.

Vertical velocity variance (w'^2) exhibits a weak dependence on domain size and resolution and a stronger dependence on aspect ratio (Fig. 2d). The spin-up run m_{fine} reproduces the observations best. The run $l_{1:5}$ exhibits the highest vertical velocity variance values among the spin-up runs, and overestimates mid-BL observations. The spin-up runs miss two isolated data points in the lower BL. The third moment of vertical velocity (w'^3) exhibits a weak dependence on domain size, resolution, and aspect ratio, with negative values throughout the BL (Fig. 2e). The negative values and the small differences between w'^3 indicate a similar closed-cell BL dynamical structure throughout the spin-up runs, with broad, slow updrafts in the cell centers, and narrow, stronger downdrafts along the cell periphery. The spin-up runs consistently underestimate observed w'^3, which exhibits positive values in the lower BL. The observed positive values of w'^3 in the lower BL indicate a stronger role of the surface sensible heat flux in driving dynamics in the observed BL relative to the spin-up runs.

The vertical distribution of TKE shows little dependence on domain size, resolution, and aspect ratio (Fig. 2f). In contrast, TKE production by buoyancy weakens at higher resolution and strengthens at a reduced aspect ratio (Fig. 2g). Because the TKE vertical profiles are nearly identical (Fig. 2f), the higher resolution spin-up runs dissipate TKE at a slower pace, and the reduced aspect ratio spin-up runs at a faster pace. Buoyancy production of TKE dominates dynamics of the boundary layer except in the lowermost 100 m, where shear production of TKE is strongest (Fig. 2h). Near-surface production of TKE by shear increases at both higher resolution and reduced aspect ratio.

The comparison of total water, cloud water, and vertical velocity variance with DYCOMS II RF01 observations (Fig. 2b–d) implies that at the aspect ratio of 1 : 10, competing effects in the model approximately compensate each other. The smaller aspect ratio of 1 : 5 produces a less favorable comparison with observations, owing to mixing at the inversion and associated exessive drying of the boundary layer. While recognizing uncertainty in the observations, we use the aspect ratio of 1 : 10 in the simulations in this work.

Discussion Paper | Discussion Paper | Discussion Paper | Discussion Paper |

This is not new.

why did you homogenize sfc fluxes?

perhaps not homog. the fluxes in the no-wind case would be a simpler exp. design.

2.2 Simulations

The simulations are listed in Table 2; they are labeled with the letters M (medium) and L (large) which denote domain size. The reference resolution is $dx = dy = 150\,m$, $dz \approx 15\,m$, $dt = 1.5\,s$, select simulations were conducted with double resolution ($dx = dy = 75\,m$, $dz \approx 7.5\,m$, $dt = 0.75\,s$). We ran simulations with the following geostrophic wind speeds: a low wind speed ($U = 5.25\,m\,s^{-1}$, $V = -4.13\,m\,s^{-1}$), the DYCOMS II RF01 wind speed ($U = 7.00\,m\,s^{-1}$, $V = -5.50\,m\,s^{-1}$, Stevens et al., 2005), and a high wind speed ($U = 8.75\,m\,s^{-1}$, $V = -6.88\,m\,s^{-1}$). High (low) geostrophic wind speed is indicated with a +(−) superscript in the simulation symbol, respectively; the DYCOMS II RF01 geostrophic wind speed is denoted with the superscript 0. We conducted sets of simulations to investigate the following phenomena:

- Effect of insolation: to identify the effect of insolation over the diurnal cycle in the simulations $M^{-,0,+}$, we ran simulations with perpetual night conditions ($M^{-,0,+}_{dark}$). Perpetual night conditions were implemented by disabling short-wave radiation.
- Buoyancy and shear-driven circulation: to identify the effect of buoyant and shear production of TKE in the simulations $L^{-,0,+}$, we conducted the simulations $\bar{L}^{-,0,+}_{buoy}$ with zero geostrophic wind speed, driven by spatially homogenized surface sensible heat and moisture fluxes from the simulations $L^{-,0,+}$, respectively. To factor out the small effect of spatial homogenization on boundary layer properties, we conducted the simulations $\bar{L}^{-,0,+}$. These are identical to $L^{-,0,+}$ but are driven with the spatially homogenized surface sensible heat and moisture fluxes from the latter. In $\bar{L}^{-,0,+}$ (as in $L^{-,0,+}$), dynamics is driven by both buoyant production of TKE and by shear production of TKE due to the geostrophic wind. In $\bar{L}^{-,0,+}_{buoy}$, dynamics is driven only by buoyant production of TKE. The effect of buoyant and shear production of TKE is discussed based on the comparison of $\bar{L}^{-,0,+}$ and $\bar{L}^{-,0,+}_{buoy}$.

3 Results and discussion

3.1 Wind speed and the diurnal cycle

The goal of this section is to identify and explain the mechanisms by which wind speed acts on the evolution of boundary layer growth, entrainment, decoupling, LWP, and cloud radiative effect (CRE) in the course of the diurnal cycle. Figures 3 and 4 show time series from the simulations $M^{-,0,+}$, which have a diurnal insolation cycle, and from the perpetual night simulations $M^{-,0,+}_{dark}$. The time series from $M^{-,0,+}_{dark}$ serve to identify the role of insolation in the simulations $M^{-,0,+}$. The time periods A, B, C, and N are highlighted to facilitate the discussion. The periods A, B, and C are defined based on time series from the simulations $M^{-,0,+}$ as follows: period A, which commences at sunrise, is characterized by a peak in LWP (Fig. 4a), period B by a peak in cloud radiative effect (Fig. 4c), and period C, which ends at sunset, by a peak in decoupling (Fig. 3j). The period N covers 1 h during nighttime (10:20–11:20 UT) when the surface sensible heat flux in the different wind speed simulations is nearly identical, so that its role as a dynamical driver can be factored out from the analysis.

3.1.1 Surface sensible heat and moisture fluxes and decoupling

Figure 3a shows the wind speed 10 m a.s.l. The 10 m wind speed is largely determined by the prescribed geostrophic wind speed and the Coriolis effect, which results in an oscillation with a period of 24 h. In the simulations with a diurnal cycle ($M^{-,0,+}$), the 10 m wind speed is suppressed during daytime relative to the simulations with perpetual night conditions ($M^{-,0,+}_{dark}$). This daytime suppression increases with wind speed and is a result of daytime decoupling.

All else equal but wind speed, the surface sensible heat and moisture fluxes would increase (decrease) with higher (lower) wind speed. This is not the case for the surface sensible heat flux: after an initial adjustment (04:00–10:50 UT), the surface sensible heat flux is anticorrelated with wind speed (Fig. 3b). Wind speed and surface moisture

flux are, however, correlated throughout the simulations (Fig. 3c). Both surface sensible heat and moisture fluxes are suppressed during daytime in the simulations with a diurnal cycle ($M^{-,0,+}$), relative to those without ($M^{-,0,+}_{\mathrm{dark}}$).

To understand the wind speed response of the surface sensible heat and moisture fluxes, surface layer temperature and water vapor need to be considered in addition to wind speed. The surface sensible heat ($F^{\mathrm{h}}_{\mathrm{surface}}$) and moisture ($F^{q}_{\mathrm{surface}}$) fluxes are calculated from the total horizontal wind speed $|\boldsymbol{U}+\boldsymbol{V}|$ in the surface layer:

are these local, grid point values?

$$F^{\mathrm{h}}_{\mathrm{surface}} \propto \Delta T |\boldsymbol{U}+\boldsymbol{V}|_{\mathrm{surface}}, \quad (3)$$

$$F^{q}_{\mathrm{surface}} \propto \Delta q_{\mathrm{v}} |\boldsymbol{U}+\boldsymbol{V}|_{\mathrm{surface}}. \quad (4)$$

$\boldsymbol{U}$ and $\boldsymbol{V}$ are the component vectors of the horizontal wind speed in the west-east and south-north directions, respectively; ΔT is the difference between the sea surface temperature and the surface layer air temperature; Δq_{v} is the difference between the saturation water vapor mixing ratio at the sea surface temperature and the surface layer water vapor mixing ratio. The drivers of the surface sensible heat and moisture fluxes are hence surface layer temperature, surface layer water vapor, and surface wind speed.

Figure 3d and e show the evolution of surface layer temperature and water vapor. The surface layer becomes warmer (Fig. 3d) and moister (Fig. 3e) with increasing wind speed. This surface warming and moistening counteracts the effect of higher wind speed on the surface sensible heat and moisture fluxes. In the case of the surface sensible heat flux (Fig. 3b) the effect of warming outbalances ($t \gtrapprox$ 10:50 UT) the effect of higher wind speed, and the surface sensible heat flux becomes suppressed at higher wind speed. The suppression of the surface sensible heat flux by surface warming is magnified by insolation in the simulations with a diurnal cycle ($M^{-,0,+}$), relative to those with perpetual night conditions ($M^{-,0,+}_{\mathrm{dark}}$). The surface moisture flux (Fig. 3c) is also reduced during daytime in the simulations with a diurnal cycle ($M^{-,0,+}$), relative to those with perpetual night conditions ($M^{-,0,+}_{\mathrm{dark}}$). We shall first focus on the general

why?

surface warming and moistening with increasing wind speed, and begin with the connection of wind speed and surface warming (Fig. 3d), followed by the connection of wind speed and surface moistening (Fig. 3e). We then will discuss daytime warming and decoupling.

Figure 3f shows the heating of the boundary layer from absorption of short-wave radiation, Fig. 3g the heating of the boundary layer from short- and long-wave radiation, latent heat release and uptake, and from the surface sensible heat flux. Following the initial adjustment (04:00–10:50 UT), higher wind speed acts to cool, while lower wind speed acts to warm the boundary layer via the combined action of these mechanisms. The general warming of the surface layer with wind speed (and of the boundary layer as a whole, not shown) therefore arises by the remaining mechanism, enhanced entrainment of warm air from the free troposphere at higher wind speed. Indeed, the boundary layer grows faster and thereby entrains more FT air at higher wind speed: Fig. 3h shows the temporal evolution of the mean inversion height $\bar{z}_{\mathrm{i}}$ as a function of wind speed, and Fig. 3i the associated mean entrainment velocity

good

$$v_{\mathrm{e}} = \frac{\mathrm{d}\bar{z}_{\mathrm{i}}}{dt} + \delta \cdot \bar{z}_{\mathrm{i}}. \quad (5)$$

The general moistening of the surface layer with wind speed (Fig. 3e) is caused by a higher surface moisture flux (Fig. 3c) in response to higher surface wind speed (Fig. 3a), and in part by greater dynamical decoupling of the cloud layer and the surface at higher wind speed. We quantify decoupling with the decoupling index

good

why does decoupling increase with wind speed?

$$\frac{\bar{z}_{\mathrm{b}} - \bar{z}_{\mathrm{LCL}}}{\bar{z}_{\mathrm{b}}}, \quad (6)$$

where $\bar{z}_{\mathrm{b}}$ is the mean cloud base altitude and $\bar{z}_{\mathrm{LCL}}$ the mean lifting condensation level altitude. Decoupling renders vertical transport of moisture from the surface to cloud base less efficient. Since decoupling increases with wind speed (Fig. 3j), it contributes to higher surface moisture at higher wind speed.

During daytime, the surface layer is warmer and the boundary layer more decoupled in the simulations $M^{-,0,+}$ relative to the simulations $M^{-,0,+}_{\mathrm{dark}}$ (Fig. 3d and j). The mechanism underlying daytime decoupling (Turton and Nicholls, 1987) has been documented (Wood, 2012, and references therein). The daytime surface warming is caused by insolation rather than by entrainment warming, because entrainment weakens during daytime in the simulations $M^{-,0,+}$ relative to $M^{-,0,+}_{\mathrm{dark}}$ (Fig. 3i). In response to the warmer surface layer, the daytime surface sensible heat flux is suppressed in the simulations $M^{-,0,+}$ relative to $M^{-,0,+}_{\mathrm{dark}}$. Daytime decoupling is also clearly apparent in surface layer moisture (Fig. 3e) in the diurnal cycle simulations $M^{-,0,+}$ when compared with the perpetual night simulations $M^{-,0,+}_{\mathrm{dark}}$: the simulations $M^{-,0,+}$ produce a moister daytime surface layer relative to the simulations $M^{-,0,+}_{\mathrm{dark}}$, despite a lower daytime surface moisture flux (Fig. 3c). This enhanced moistening of the surface layer (Fig. 3f) suppresses the daytime surface moisture flux (Fig. 3c) via Eq. (4).

3.1.2 Wind speed as driver of boundary layer growth and entrainment

Here we identify the mechanism by which higher wind speed drives faster boundary layer growth and stronger entrainment. Since increasing wind speed results in higher LWP (Fig. 4a), one may be lead to assume that at higher wind speed, stronger cloud top long-wave emissions drive additional TKE production, which in turn drives stronger entrainment. However, LW cooling of stratocumulus clouds becomes very insensitive to LWP for $50\,\mathrm{g\,m^{-2}} \lessapprox \mathrm{LWP} \leq 250\,\mathrm{g\,m^{-2}}$ (Petters, 2009). We will show that wind speed drives faster boundary layer growth and stronger entrainment by enhancing TKE production from latent heat release in cloud layer updrafts. Figure 5 shows LW heating (a), latent heating (b), and TKE net production by buoyancy (c) and shear (d) as functions of the normalized height $z/\bar{z}_{\mathrm{i}}$, averaged over the period N (10:20–11:20 UT) from the simulations $M^{-,0,+}$, separated by updrafts and downdrafts. The surface sensible heat flux is nearly identical in the different wind speed simulations in period N (Fig. 3b), and its role can be factored out from the analysis. The conclusions are valid at later times,

because increasing wind speed suppresses the surface sensible heat flux following the period N (Fig. 3b), so that the surface sensible heat flux cannot account for higher boundary layer growth and stronger entrainment. The layers L_1 ($0.925 \leq z/\bar{z}_{\mathrm{i}} < 1.0375$) and L_2 ($0.625 \leq z/\bar{z}_{\mathrm{i}} < 0.925$) are highlighted to facilitate the discussion. Layer L_1 contains most of the LW cooling (Fig. 5a) and some latent heating and cooling (Fig. 5b). In layer L_2, latent heating/cooling dominates over LW heating/cooling.

LW heating/cooling does not respond to wind speed (Fig. 5a). Latent cooling of downdrafts in layer L_1 shows no systematic response to wind speed, while latent heating of updrafts in layer L_1 shows a weak increase with wind speed (Fig. 5b). This absence of a clear wind speed signal in layer L_1 turns the focus to layer L_2. In its lower part, latent heating increases more in the updrafts than latent cooling in the downdrafts in response to increasing wind speed. More importantly, TKE net production by buoyancy shows a positive response to wind speed only in the updrafts of layer L_2 (Fig. 5c). Since in layer L_2, latent heating/cooling dominates over LW heating/cooling, we deduce that wind speed drives boundary layer growth and entrainment by boosting latent heat release and buoyant production of TKE in cloud updrafts, in response to the higher surface moisture flux at higher wind speed. This mechanism is similar to the deepening-warming decoupling process (Bretherton, 1992; Bretherton and Wyant, 1997; Wyant et al., 1997), in which an increasing sea surface temperature drives a stronger surface moisture flux, which generates more TKE within the cloud layer and thereby enhances entrainment.

Figure 5d shows TKE net production by shear. Near the surface, shear drives a stronger circulation at higher wind speed. At the inversion, in layer L_1, shear also contributes to a stronger circulation with increasing wind speed. This latter contribution could enhance entrainment at higher wind speed, although it is clearly weaker than the increase with wind speed of TKE net production from buoyancy in updrafts of layer L_2 (Fig. 5c). The relative roles of buoyancy- and shear-driven circulation in driving the evolution of the boundary layer will be discussed in Sect. 3.2, where we show

The (updraft) mass flux profile might provide a useful measure of the changes in BL circulation. See Krueger et al. 1995a,b for examples. These studies were the first to document the deepening stage of the stratocumulus to cumulus transition.

As far as the BL circulation is concerned, it is no different! The BL sees only the surface fluxes, not the components that produce it.

quantify using mass flux profile

Circulation is ambiguous. I don't think it is synonymous with TKE however. I think instead of mass flux as being a measure of circulation.

that buoyancy-driven circulation is the fundamental mechanism of enhanced boundary layer growth and entrainment at higher wind speed.

3.1.3 Wind speed and LWP, cloud fraction, and cloud radiative effect

Figure 4a–c shows LWP, cloud fraction, and total (short-wave + longwave) cloud radiative effect (CRE) from the simulations $M^{-,0,+}$ and $M^{-,0,+}_{\mathrm{dark}}$. LWP increases with wind speed (Fig. 4a) throughout the perpetual night simulations ($M^{-,0,+}_{\mathrm{dark}}$), via the wind speed enhancement of the surface moisture flux (Fig. 3c). Insolation suppresses LWP during daytime in the simulations $M^{-,0,+}$, which creates a LWP peak in the early morning hours (period A). Both LWP morning peak and daytime suppression increase with wind speed. Wind speed hence accentuates the diurnal LWP cycle by expanding the morning – afternoon contrast. Cloud fraction (Fig. 4b) is suppressed during daytime by insolation as well. At higher resolution, daytime suppression of cloud fraction becomes smaller and less dependent on wind speed, while our other findings remain unaffected (Appendix C).

LWP, cloud fraction, and insolation co-determine the CRE (Fig. 4c). Neither factor dominates, and CRE peaks in period B, following the morning LWP peak (period A, Fig. 4a) but before the midday insolation peak (early period C, Fig. 3f). At the time of the CRE peak, LWP is enhanced at higher wind speed (Fig. 4a), hence the CRE strengthens with wind speed. In the course of the day, however, LWP (Fig. 4a) and cloud fraction (Fig. 4b) fall more rapidly at higher wind speed, and afternoon CRE values (period C) at high wind speed approach those of the low and reference wind speed simulations.

Table 3 gives the CRE averaged over the 24 h duration of the simulations, from the simulations $M^{-,0,+}$ with the reference resolution, and from the simulations $M^{-,0,+}_{\mathrm{fine}}$ with double resolution in each dimension. The diurnally averaged CRE increases with wind speed at both resolutions. However, with increasing wind speed, CRE becomes less sensitive to wind speed. The reason is the stronger suppression of LWP in the after-

noon at higher wind speed, which also suppresses the CRE (Fig. 4c). Notably, both the diurnally averaged CRE and its response to wind speed depend on resolution. The effect of resolution is documented in Appendix C.

3.1.4 Wind speed enhanced daytime suppression of LWP

We will now examine the enhanced daytime LWP suppression at higher wind speed in the simulations $M^{-,0,+}$ (Fig. 4a). We will conclude that during daytime, despite higher decoupling and a reduced moisture flux in cloud base updrafts at higher wind speed, buoyant TKE production in cloud level updrafts increases with wind speed and drives additional entrainment, causing stronger cloud water evaporation and LWP reduction. We shall first discuss daytime decoupling and proceed to the action of wind speed.

Insolation in the simulations $M^{-,0,+}$ warms the cloud layer (Fig. 3k) more than the sub-cloud layer (Fig. 3l), because absorption by cloud water and water vapor at cloud level reduces the amount of short-wave radiation reaching the sub-cloud layer. The warming of the cloud layer reduces LWP (Fig. 4a) and stabilizes the boundary layer. Daytime TKE production falls in the simulations $M^{-,0,+}$ (Fig. 4f) mainly as a result of reduced TKE production by buoyancy (Fig. 4g), as TKE production by shear varies only weakly during daytime (Fig. 4h). The resulting warmer (Fig. 3d), more weakly driven (Fig. 4f), and more decoupled (Fig. 3j) daytime circulation in the simulations $M^{-,0,+}$ suppresses surface wind speed (Fig. 3a) and the surface sensible heat and moisture flux (Fig. 3b and c) relative to the simulations $M^{-,0,+}_{\mathrm{dark}}$. Still, a higher wind speed drives a higher surface moisture flux in the simulations $M^{-,0,+}$ (Fig. 3c), as well as a higher cloud base moisture flux (Fig. 4d). However, the moisture flux in cloud base updrafts decreases with increasing wind speed in the simulations $M^{-,0,+}$ during the daytime period B and C (Fig. 4e). Nonetheless, TKE production by buoyancy in cloud layer updrafts increases with wind speed during the period B and C (Fig. 4i), and is the only buoyancy-driven TKE production term that increases with wind speed at all times (Fig. 4i–l). Hence, wind speed drives boundary layer growth and entrainment by boost-

why doesn't the enhanced entrainment counteract the surface flux increase and decrease the LWP? You should explain this.

too much detail?

summarize instead.

It is the decoupling that increases conditional instability and updraft speed.

The radiative warming is distributed throughout the BL if the BL is not decoupled. Decoupling restricts the warming to the upper layer, but not because it is cloudy.

This is a consequence or even a definition of decoupling (actually, not completely decoupled).

??

why?

why?

Such a scenario does not occur in simulations of the transition to cumulus as the surface latent heat flux increases due to SST increase, so it should not happen due to wind speed increase.

ing buoyant production of TKE in cloud updrafts even in decoupled daytime conditions, when stronger decoupling at higher wind speed leads to a reduced moisture flux in cloud base updrafts. Although the buoyant production of TKE due to latent heat release in cloud layer updrafts drives additional entrainment at higher wind speed, the associated formation of cloud water is insufficient to compensate cloud water evaporation from higher entrainment drying and warming at higher wind speed, and LWP is progressively suppressed during daytime as wind speed increases (Fig. 4a). This mechanism could potentially result in a runaway breakup of the cloud, or initiate or assist in the transition from stratocumulus to shallow cumulus along a gradient in sea surface temperature (Bretherton, 1992; Bretherton and Wyant, 1997; Wyant et al., 1997).

3.2 Buoyancy- and shear-driven dynamics

This section discusses the role of buoyancy- and shear-driven dynamics (due to the geostrophic wind) for the properties and evolution of the boundary layer. The goal is to identify the role of buoyancy- and shear-driven dynamics in boundary layer growth and entrainment at different wind speeds, and the mechanism by which shear due to the geostrophic wind modulates decoupling in the course of the diurnal cycle. We limit the discussion to phenomenological aspects of buoyancy and shear effects, noting that the interaction of buoyancy- and shear-driven dynamics and the underlying mechanisms and causal relationships lend themselves to in-depth investigation beyond the scope of this work.

3.2.1 Dynamical support of boundary layer growth and entrainment

Figure 6 shows time series from the simulations $\bar{L}^{-,0,+}_{\mathrm{buoy}}$ and $\bar{L}^{-,0,+}$. The 10 m wind speed in the simulations $\bar{L}^{-,0,+}_{\mathrm{buoy}}$ has no geostrophic component and is hence lower than in the simulations $\bar{L}^{-,0,+}$ (Fig. 6a), while as prescribed, the surface sensible heat and moisture fluxes are identical (Fig. 6b and c). The action of buoyancy- and shear-driven

dynamics appears in the decoupling index, inversion height, entrainment velocity, and LWP (Fig. 6d–g).

During the night and in the morning, $\bar{L}^{-,0,+}_{\mathrm{buoy}}$ is characterized, relative to $\bar{L}^{-,0,+}$, by faster boundary layer growth (Fig. 6e) and stronger entrainment (Fig. 6f). It is hence buoyancy-driven dynamics, rather than shear-driven dynamics that translates faster geostrophic wind into faster boundary layer growth and stronger entrainment during the night and in the morning. This becomes most apparent by considering entrainment velocity v_{e} (Eq. 5) averaged over period N (Fig. 6f): in the simulations with buoyancy-driven dynamics ($\bar{L}^{-,0,+}_{\mathrm{buoy}}$), v_{e} increases from $\bar{L}^{-}_{\mathrm{buoy}}$ to $\bar{L}^{0}_{\mathrm{buoy}}$ by $0.40\,\mathrm{mm\,s^{-1}}$, and from $\bar{L}^{0}_{\mathrm{buoy}}$ to $\bar{L}^{+}_{\mathrm{buoy}}$ by $0.52\,\mathrm{mm\,s^{-1}}$. Including the effect of shear from geostrophic wind ($\bar{L}^{-,0,+}$) reduces the response of v_{e} to wind speed: it only increases from $\bar{L}^{-}$ to $\bar{L}^{0}$ by $0.35\,\mathrm{mm\,s^{-1}}$, and from $\bar{L}^{0}$ to $\bar{L}^{+}$ by $0.42\,\mathrm{mm\,s^{-1}}$. Since the surface sensible heat flux is nearly independent of wind speed during period N (Fig. 6b), enhanced boundary layer growth and entrainment at higher wind speed can be exclusively tied to higher TKE production from latent heat release in cloud updrafts at higher wind speed (Sect. 3.1.2), with overall TKE production from shear due to the geostrophic wind speed acting against it. This analysis does not distinguish between the effects of higher shear production of TKE at higher wind speed at the surface and at the inversion (Fig. 5d), and therefore does not determine whether shear production of TKE at the inversion due to geostrophic wind supports entrainment, as locally generated shear does (Wang et al., 2008, 2012; Katzwinkel et al., 2012; Mellado et al., 2014).

A more complex picture of the role of buoyancy- and shear-driven dynamics emerges in the afternoon (period C). At low and reference wind speed, shear due to geostrophic wind renders the boundary layer more decoupled, but the opposite is the case at high wind speed (Fig. 6d). Concurrently, presence of shear from geostrophic wind enhances LWP in period C at all wind speeds (Fig. 6g). Shear production of TKE due to geostrophic wind therefore modulates decoupling and thereby the transport of moisture between the surface and cloud base in the course of the day.

how?

This is difficult to follow.

3.2.2 Modulation of decoupling by geostrophic wind in the course of the diurnal cycle

During nighttime and for several hours into daytime, the boundary layer is more decoupled in the simulation $\bar{L}^{-,0,+}$ compared to the simulations $\bar{L}^{-,0,+}_{\mathrm{buoy}}$ (Fig. 6d). Since in the simulations $\bar{L}^{-,0,+}_{\mathrm{buoy}}$, TKE is not produced from shear due to geostrophic wind, the cause of higher nighttime decoupling at higher wind speed is stronger entrainment (Fig. 6f). A role of boundary layer deepening with wind speed (Fig. 6e) can be excluded because nighttime decoupling remains nearly constant at each wind speed (Fig. 6d), despite a progressive deepening of the boundary layer. Consequently, the cause of higher nighttime decoupling at higher wind speed in the simulations $\bar{L}^{-,0,+}$ is the combined action of stronger entrainment and stronger production of TKE from shear due to geostrophic wind. In the afternoon (period C), however, shear from geostrophic wind acts to maintain higher LWP relative to the simulations without shear (Fig. 6g), and in the high wind speed case, reduces decoupling (Fig. 6d).

We will identify the mechanism underlying the modulation of boundary layer decoupling by shear-driven dynamics due to geostrophic wind. The decoupling index (Eq. 6) is defined based on the altitude difference between the lifting condensation level and cloud base. The decoupling index is > 0 when the sub-cloud layer circulation does not efficiently transport moisture from the surface to cloud base. Noting that in the sub-cloud layer, $q_{\mathrm{v}} = q_{\mathrm{t}}$, we shall employ the quantity

$$\zeta_{q_{\mathrm{t}}} \doteq -\mathrm{d}\bar{q}_{\mathrm{t}}/\mathrm{d}z, \tag{7}$$

the negative value of the vertical gradient of the horizontally averaged total water mixing ratio $\bar{q}_{\mathrm{t}}$, to measure the efficiency of vertical moisture transport. $\zeta_{q_{\mathrm{t}}} = 0$ indicates perfect mixing, $\zeta_{q_{\mathrm{t}}} > 0$ inefficient upward moisture transport by resolved scale dynamics, subgrid-scale mixing, and physical and numerical diffusion.

Figure 7 shows vertical profiles averaged over the period N (10:20–11:20 UT) from the simulations $\bar{L}^{-,0,+}$ and $\bar{L}^{-,0,+}_{\mathrm{buoy}}$. During this period, shear due to geostrophic wind

a lot of details make it hard to follow.

too much detail.

causes higher decoupling (Fig. 6d). Total water q_{t} (Fig. 7a) and $\zeta_{q_{\mathrm{t}}}$ (Fig. 7b) show that the efficiency of upward moisture transport in the sub-cloud layer decreases with increasing wind speed or in the presence of shear-driven dynamics due to the geostrophic wind: as wind speed increases or when shear due to geostrophic wind is present, more moisture accumulates near the surface (Fig. 7a), and $\zeta_{q_{\mathrm{t}}}$ assumes larger values (Fig. 7b). The cause of reduced efficiency of vertical moisture transport in the sub-cloud layer is hence shear due to geostrophic wind. Shear-driven circulation near the surface also interferes with buoyancy-driven circulation (Fig. 7c and d): in the layer L_3, in the presence of TKE production by shear from geostrophic wind, buoyant production of TKE is suppressed.

Figure 8 shows vertical profiles averaged over the afternoon period 22:30–23:30 UT from the simulations $\bar{L}^{-,0,+}$ and $\bar{L}^{-,0,+}_{\mathrm{buoy}}$. During this period, shear due to geostrophic wind reduces decoupling at high wind speed (Fig. 6d). This shapes the q_{t} profiles (Fig. 8a): q_{t} is higher near the surface in the simulations $\bar{L}^{-,0}$ than in the simulations $\bar{L}^{-,0}_{\mathrm{buoy}}$; at high wind speed however, q_{t} is lower near the surface in the simulation $\bar{L}^{+}$ than in the simulations $\bar{L}^{+}_{\mathrm{buoy}}$. Clearly, at high wind speed and in the presence of shear due to geostrophic wind, vertical moisture tranport in the sub-cloud layer is more efficient at this time of day. The $\zeta_{q_{\mathrm{t}}}$ profiles provide a more differentiated picture of the action of shear due to geostrophic wind at the three different wind speeds (Fig. 8b): at low wind speed, vertical moisture transport is less efficient in the presence of shear due to geostrophic wind ($\bar{L}^{-}$) than in its absence ($\bar{L}^{-}_{\mathrm{buoy}}$) throughout the sub-cloud layer ($z/\bar{z}_{\mathrm{i}} = 0$ to $z/\bar{z}_{\mathrm{i}} \approx 0.625$). At reference wind speed, shear in the simulation $\bar{L}^{0}$ renders vertical moisture transport more efficient in the upper part of the sub-cloud layer ($z/\bar{z}_{\mathrm{i}} \approx 0.4$ to $z/\bar{z}_{\mathrm{i}} \approx 0.625$) relative to the shearless simulation $\bar{L}^{0}_{\mathrm{buoy}}$. At high wind speed, shear in the simulation $\bar{L}^{+}$ renders vertical moisture transport more efficient throughout the sub-cloud layer ($z/\bar{z}_{\mathrm{i}} = 0$ to $z/\bar{z}_{\mathrm{i}} \approx 0.625$) relative to the simulation $\bar{L}^{+}_{\mathrm{buoy}}$.

We note that shear due to geostrophic wind has little effect on TKE net production due to buoyancy in the afternoon period 22:30–23:30 UT (Fig. 8c) except at high wind

a lot of detail. maybe a schematic diagram would be helpful.

speed ($\bar{L}^{+}$ and $\bar{L}^{+}_{buoy}$), where it suppresses TKE net production due to buoyancy to values close to zero in the sub-cloud layer (L_3), while enhancing it at cloud level (L_2). With the very low TKE production due to buoyancy in the sub-cloud layer in the high wind speed conditions, shear due to geostrophic wind becomes the dominant source of TKE at high wind speed between the surface and cloud base ($z/\bar{z}_i = 0$ to $z/\bar{z}_i \approx 0.625$, Fig. 8d). The conclusion is that with increasing wind speed at strong decoupling (period C in Fig. 6d), the shear-driven circulation due to geostrophic wind takes over from buoyancy-driven circulation in maintaining vertical moisture transport in the sub-cloud layer. By securing moisture tranport between the surface and cloud base, it helps maintain LWP and supports buoyant TKE production at cloud level: in cloud updrafts (layer L_2), the highest TKE net production by buoyancy is present in the high wind speed simulation $\bar{L}^{+}$ (Fig. 8c).

3.2.3 Cloud layer updrafts as dynamical drivers of entrainment

A corollary of the comparison between the simulations without ($\bar{L}^{-,0,+}_{buoy}$) and with ($\bar{L}^{-,0,+}$) shear due to geostrophic wind is that boundary layer growth and entrainment are not tied to total boundary layer TKE: over much of the diurnal cycle, dynamics in the simulations $\bar{L}^{-,0,+}_{buoy}$ supports faster boundary layer growth and higher entrainment (Fig. 6e and f) with lower boundary layer TKE relative to the simulations $\bar{L}^{-,0,+}$ (Fig. 6h). The additional boundary layer TKE in the simulations $\bar{L}^{-,0,+}$, relative to the simulations $\bar{L}^{-,0,+}_{buoy}$, originates from shear production due to the geostrophic wind. Hence features of boundary layer dynamics that are not represented by total boundary layer TKE constitute the key driver of entrainment. Figure 6i shows the time series of the TKE vertical component

$$TKE_w = \frac{w'^2}{2} \quad (8)$$

w_e is more commonly used

this is well known.

in updrafts of the cloud layer. Comparison of TKE_w (Fig. 6i) and of entrainment velocity v_e (Fig. 6f) shows that these two quantities behave in unison in the course of the diurnal cycle, in response to wind speed, and in response to the presence of shear due to geostrophic wind: in nighttime conditions, and for several hours into daytime, both TKE_w and v_e increase with wind speed, but are suppressed by the action of shear due to geostrophic wind. Both quantities experience a suppression during daytime (period C). During period C at high wind speed, shear due to geostrophic wind increases both TKE_w and v_e, in contrast to its suppressing effect in nightime conditions.

In Sect. 3.1.2, we found that wind speed drives boundary layer growth and entrainment by boosting buoyant production of TKE from latent heat release in cloud updrafts. This, together with the concomitant behavior of cloud updraft TKE_w and v_e in the course of the diurnal cycle, in response to wind speed, and to the presence/absence of shear due to geostrophic wind suggests that cloud layer updrafts are a key dynamical driver of boundary layer growth and entrainment. However, because the evolution and behavior of cloud updraft TKE_w and v_e is not identical (Fig. 6f and i), additional factors determining the entrainment velocity v_e likely exist.

4 Conclusions

Observations have identified global and regional trends towards faster surface wind speed over the oceans in the 20th century (Young et al., 2011; Hande et al., 2012; Bertin et al., 2013; Servain et al., 2014). These trends are not necessarily a consequence of climate change, but could arise from internal climate variability (Dobrynin et al., 2015). Concurrently, climate simulations predict changes in ocean wind speeds in the course of the 21st century (McInnes et al., 2011; Hemer et al., 2013). Wind speed drives the surface fluxes of sensible heat, moisture, and momentum, and thereby impacts cloud liquid water path and cloud radiative properties. Long-term changes in large scale wind speed and the associated cloud response therefore constitute a cloud-

These are the transient responses! For climate change, need the equilibrium responses, as in the recent Dutch paper.

can this be quantified with a generalized turbulence velocity scale like Moeng and Sullivan proposed for the CBL?

already well known

climate feedback mechanism, with the potential to impact Earth's radiation budget, the formation of precipitation, and the effect of aerosol on clouds.

We have investigated the response of non-precipitating, overcast marine stratocumulus clouds to changes in large scale wind speed, all else equal. The goal of the investigation was to identify and explain the dynamical processes by which wind speed acts on the evolution of boundary layer growth, entrainment, decoupling, liquid water path (LWP), and cloud radiative effect in the course of a diurnal cycle. Furthermore, we explored the role of buoyancy- and shear-driven dynamics for boundary layer growth, entrainment, decoupling, and LWP at different wind speeds. We focused on the dynamical rather than the microphysical response of the stratocumulus-topped boundary layer to changes in wind speed, and excluded the effect of wind speed on surface aerosol production and loss.

We used cloud-system resolving simulations which were initialized with boundary layer properties, cloud properties, and dynamics from observations. Owing to identical initial and boundary conditions, the simulations are suited to identify and characterize the mechanisms by which the stratocumulus-topped marine boundary layer responds to different wind speeds. However, they do not represent a stratocumulus-topped marine boundary layer in a future climate at different wind speeds, which would require initial and boundary conditions that are consistent with the chosen climate and wind speeds. The results and their analysis are therefore specific for the cloud state and the initial and boundary conditions considered.

We find that higher wind speed leads to faster boundary layer growth and entrainment. The dynamical driver is enhanced buoyant production of turbulence kinetic energy (TKE) from latent heat release in cloud updrafts. Concomitant behavior of the cloud updraft vertical component of TKE and of entrainment velocity in the course of the diurnal cycle, in response to wind speed, and in response to the presence or absence of shear due to geostrophic wind suggests that cloud updrafts are a key dynamical driver of boundary layer growth and entrainment. However, additional factors determining entrainment likely exist.

Higher wind speed enhances LWP during the night and in the morning, and more strongly suppresses it later in the day. Wind speed hence accentuates the diurnal LWP cycle by expanding the morning – afternoon contrast. The higher LWP at higher wind speed does not, however, enhance cloud top cooling because in clouds with LWP $\gtrapprox 50\,\mathrm{g\,m^{-2}}$, long wave emissions are very insensitive to LWP. This leads to the more general conclusion that in sufficiently thick stratocumulus clouds, additional boundary layer growth and entrainment due to a boundary layer moistening arises by stronger production of TKE from latent heat release in cloud updrafts, rather than from enhanced longwave cooling.

We find that large scale wind plays an important role in modulating boundary layer decoupling. At nighttime and at low wind speed during daytime, it enhances decoupling in part by faster boundary layer growth and stronger entrainment, and in part because circulation driven by shear from large scale wind in the sub-cloud layer hinders vertical moisture transport between the surface and cloud base. With increasing wind speed, however, in decoupled daytime conditions, shear-driven circulation due to large scale wind takes over from buoyancy-driven circulation in transporting moisture from the surface to cloud base, and thereby reduces decoupling and helps maintain LWP.

The cloud radiative effect (CRE) is sensitive to wind speed. Owing to the wind speed enhancement of LWP during the night and in the morning, higher wind speed translates to a stronger diurnally averaged CRE. The CRE response to wind speed changes, however, in the course of the day: the CRE is most sensitive to wind speed at its peak shortly before noon, and becomes insensitive to wind speed later in the day owing to the wind speed-enhanced daytime suppression of LWP. As a consequence, the diurnally averaged CRE becomes less sensitive to wind speed with increasing wind speed.

Appendix A: Nudging

We used Newtonian relaxation (e.g., Jeuken et al., 1996) of select prognostic variables to generate conditions (temperature, water content, dynamics, cloud properties)

in the final state of spin-up runs that are consistent with DYCOMS II RF01 observations (Stevens et al., 2005). The final state of spin-up runs initializes the simulations. This has the advantage (relative to an initialization with a static initial state with a prescribed total water content, present as water vapor, and with a zero cloud water content) that the simulations are not biased by the model working to establish dynamics and a cloud deck from a static state. In the simulations, we used nudging to ensure that free tropospheric potential temperature and water vapor do not drift due to subsidence, which would, among other things, increase the potential temperature jump across the inversion, and affect the boundary layer underneath.

We distinguish soft and hard nudging. In soft nudging, the nudging term of a quantity X is

$$\frac{\Delta_{\text{nudging}} X(x,y,z,t)}{\Delta t} = -\frac{\overline{X}(z,t) - X_{\text{target}}(z)}{\tau_X}. \tag{A1}$$

It is calculated from the deviation of the horizontal mean $\overline{X}(z,t)$ from the target vertical profile $X_{\text{target}}(z)$. τ_X is the nudging time constant, Δt the model time step. In hard nudging, the nudging term is calculated from the local deviation $X(x,y,z,t)$ from the target vertical profile $X_{\text{target}}(z)$:

$$\frac{\Delta_{\text{nudging}} X(x,y,z,t)}{\Delta t} = -\frac{X(x,y,z,t) - X_{\text{target}}(z)}{\tau_X}. \tag{A2}$$

In either soft and hard nudging the nudging term is passed as a tendency of X to the dynamical core of the model.

The distinction between soft and hard nudging can be motivated by considering potential temperature: under soft nudging, the surface sensible heat flux, dynamics, cloud processes, and radiative heating/cooling are permitted to modify potential temperature locally under the constraint that the domain mean profile is maintained at its target value. In hard nudging, the action of these processes would be suppressed and potential temperature would maintain the target profile locally. The choice between soft and hard nudging will depend on the preferred target state.

A1 Spin-up runs

Potential temperature $\theta(x,y,z,t)$ was soft-nudged at each location (x,y,z) in the boundary layer and free troposphere in proportion to the deviation of the horizontal (z) mean liquid water potential temperature $\bar{\theta}_{\text{l}}(z,t)$ from the initial liquid water potential temperature $\theta_{\text{l}}(z,t=0)$:

$$\frac{\Delta_{\text{nudging}} \theta(x,y,z,t)}{\Delta t} = -\frac{\bar{\theta}_{\text{l}}(z,t) - \theta_{\text{l}}(z,t=0)}{\tau_\theta} \tag{A3}$$

We calculated the nudging term of θ from θ_{l} because $\theta_{\text{l}}(z,t=0) = \theta(z,t=0)$ and because θ_{l} is conserved under water phase changes. In other words, θ is nudged to maintain $\bar{\theta}_{\text{l}}(z,t)$ at its initial value $\theta_{\text{l}}(z,t=0)$. We applied hard nudging to water vapor (q_{v}) in the free troposphere (10 m higher than the inversion):

$$\frac{\Delta_{\text{nudging}} q_{\text{v}}(x,y,z,t)}{\Delta t} = -\frac{q_{\text{v}}(x,y,z,t) - q_{\text{t}}(z,t=0)}{\tau_{q_{\text{v}}}} \tag{A4}$$

In the boundary layer, the water variables (water vapor q_{v}, cloud water q_{c}, rain water q_{r}, and total water $q_{\text{t}} = q_{\text{v}} + q_{\text{c}} + q_{\text{r}}$) were not nudged in order allow the nudged mean potential temperature profile, the surface sensible heat fluxes, dynamics, radiative heating/cooling, and cloud microphysics determine their evolution.

Hard nudging was applied in the following manner to the interstitial aerosol number $\widetilde{N}_m$ and mass $\widetilde{M}_{m,n}$, both in the boundary layer and the free troposphere:

$$\frac{\Delta_{\text{nudging}} \widetilde{N}_m(x,y,z,t)}{\Delta t} = -\frac{N_m(x,y,z,t) - N_m(t=0)}{\tau_{\text{aerosol}}}$$

$$\frac{\Delta_{\text{nudging}}\widetilde{M}_{m,n}(x,y,z,t)}{\Delta t} = -\frac{M_{m,n}(x,y,z,t) - M_{m,n}(t=0)}{\tau_{\text{aerosol}}} \tag{A5}$$

The index m denotes the three log-normal aerosol modes (Aitken, accumulation, and coarse), the index n the chemical species. N_m and $M_{m,n}$ are the total aerosol number and mass, $N_m(t=0)$ and $M_{m,n}(t=0)$ their initial (and nudging target) values, respectively. Although the nudging term is calculated from the total aerosol number and mass, it is applied to interstitial aerosol only to allow cloud microphysics determine the aerosol number and mass residing inside cloud and rain drops. In the spin-up runs, the Aitken and coarse modes were held at zero number and mass. The accumulation mode number was nudged towards 300 mg^{-1}, containing 4.74 $\mu\text{g kg}^{-1}$ of sulfate, with a dry geometric mean (median) diameter of 200 µm and a geometric standard deviation of 1.5. We used the time constants $\tau_\theta = \tau_{q_\text{v}} = \tau_{\text{aerosol}} = 300$ s.

A2 Simulations

We applied soft nudging to potential temperature and water vapor in the free troposphere of the simulations:

$$\begin{aligned}\frac{\Delta_{\text{nudging}}\theta(x,y,z,t)}{\Delta t} &= -\frac{\bar{\theta}(z,t) - \theta(z,t=0)}{\tau_\theta} \\ \frac{\Delta_{\text{nudging}}q_\text{v}(x,y,z,t)}{\Delta t} &= -\frac{\overline{q}_\text{v}(z,t) - q_\text{t}(z,t=0)}{\tau_{q_\text{v}}}\end{aligned} \tag{A6}$$

In this soft nudging, potential temperature and water vapor are nudged only to the extent that their horizontal mean values deviate from the initial profiles, and are otherwise allowed to vary in response to dynamics and radiative heating/cooling. Still, as a precaution, the nudging is applied only 50 m or higher above the inversion, so as to not to interfere with processes at the inversion. No nudging is performed in the boundary layer and below 50 m above the inversion. The nudging scheme accommodates

changes in inversion height: the altitude above which nudging is applied moves up and down with the inversion. Should the inversion descend below its initial height, potential temperature and water vapor are nudged towards linear extrapolations of their initial free tropospheric profiles. This does not occur in the simulations in this work. We used the time constants $\tau_\theta = \tau_{q_\text{v}} = 300$ s. In contrast to the spin-up runs, aerosol number and mass are not nudged in the simulations.

Appendix B: Boundary layer water budget

The boundary layer water budget equation is derived. (x,y,z) form a right-handed Cartesian coordinate system with z pointing up; t is the time. The boundary layer mean water mass path (vertically integrated water mass per horizontal area) is

$$Q(t) = \frac{1}{A}\iint_A \mathrm{d}x\,\mathrm{d}y \int_0^{z_\text{i}(x,y,t)} \mathrm{d}z\,\rho(x,y,z,t) \tag{B1}$$

where ρ is the volumetric mass density of water, A is the horizontal area covered by the simulation domain, and z_i is the inversion height. The Leibniz integral rule gives

$$\frac{\mathrm{d}Q(t)}{\mathrm{d}t} = \frac{1}{A}\iint_A \mathrm{d}x\,\mathrm{d}y \int_0^{z_\text{i}(x,y,t)} \mathrm{d}z\,\frac{\partial\rho(x,y,z,t)}{\partial t} + \frac{1}{A}\iint_A \mathrm{d}x\,\mathrm{d}y\,\rho(x,y,z_\text{i},t)\frac{\partial z_\text{i}(x,y,t)}{\partial t}, \tag{B2}$$

and with the mass continuity equation

$$\frac{\partial\rho}{\partial t} = -\boldsymbol{\nabla}(\boldsymbol{v}\rho) \tag{B3}$$

one obtains

$$\frac{\mathrm{d}Q(t)}{\mathrm{d}t} = -\frac{1}{A}\iint_A \mathrm{d}x\,\mathrm{d}y \int_0^{z_\mathrm{i}(x,y,t)} \mathrm{d}z\,\boldsymbol{\nabla}(\boldsymbol{v}\rho) + \frac{1}{A}\iint_A \mathrm{d}x\,\mathrm{d}y\,\rho(x,y,z_\mathrm{i},t)\frac{\partial z_\mathrm{i}(x,y,t)}{\partial t} \tag{B4}$$

where $\boldsymbol{v}$ is water transport velocity. Applying the divergence theorem yields

$$\frac{\mathrm{d}Q(t)}{\mathrm{d}t} = -\frac{1}{A}\oiint_S \mathrm{d}\boldsymbol{s}\,\boldsymbol{v}\rho + \frac{1}{A}\iint_A \mathrm{d}x\,\mathrm{d}y\,\rho(x,y,z_\mathrm{i},t)\frac{\partial z_\mathrm{i}(x,y,t)}{\partial t} \tag{B5}$$

where S is the closed surface enveloping the boundary layer and $\mathrm{d}\boldsymbol{s}$ an outward pointing surface element. In Eq. (B5), the first term on the right hand side represents water transport across the boundary of the simulation domain, and the second term changes in boundary layer total water due to changes in the location and shape of the inversion. In a horizontally periodic simulation domain the first term reduces to the water flux at the boundary layer base (F^q_base) and at the inversion (F^q_inv):

$$-\frac{1}{A}\oiint_S \mathrm{d}\boldsymbol{s}\,\boldsymbol{v}\rho = F^q_\mathrm{base} - F^q_\mathrm{inv} \tag{B6}$$

Note that since the inversion is not a priori a horizontal plane, $\boldsymbol{F}^q_\mathrm{inv}$ does not necessarily point in z direction. We will show that the second term on the right hand side of Eq. (B5) decomposes into a part associated with the temporal change in mean inversion height $\bar{z}_\mathrm{i}$, and into a part associated with local fluctuations of the inversion height Δz_i. We define

$$z_\mathrm{i}(x,y,t) \doteq \bar{z}_\mathrm{i}(t) + \Delta z_\mathrm{i}(x,y,t), \tag{B7}$$

where $\bar{z}_\mathrm{i}(t)$ is the mean inversion height, with the local inversion height deviations having a zero mean:

$$\frac{1}{A}\iint_A \mathrm{d}x\,\mathrm{d}y\,\Delta z_\mathrm{i}(x,y,t) = 0. \tag{B8}$$

This gives

$$\frac{\partial z_\mathrm{i}(x,y,t)}{\partial t} = \frac{\mathrm{d}\bar{z}_\mathrm{i}(t)}{\mathrm{d}t} + \frac{\partial \Delta z_\mathrm{i}(x,y,t)}{\partial t}. \tag{B9}$$

Similarly, we define

$$\rho(x,y,z_\mathrm{i},t) \doteq \bar{\rho}_\mathrm{i}(t) + \Delta\rho_\mathrm{i}(x,y,t), \tag{B10}$$

where $\bar{\rho}_\mathrm{i}(t)$ is the mean volumetric mass density of water at the inversion, with the local deviations along the inversion having a zero mean:

$$\frac{1}{A}\iint_A \mathrm{d}x\,\mathrm{d}y\,\Delta\rho_\mathrm{i}(x,y,t) = 0. \tag{B11}$$

It is then straightforward to show that

$$\frac{1}{A}\iint_A \mathrm{d}x\,\mathrm{d}y\,\rho(x,y,z_\mathrm{i},t)\frac{\partial z_\mathrm{i}(x,y,t)}{\partial t} = \bar{\rho}_\mathrm{i}(t)\frac{\mathrm{d}\bar{z}_\mathrm{i}(t)}{\mathrm{d}t} + \frac{1}{A}\iint_A \mathrm{d}x\,\mathrm{d}y\,\Delta\rho_\mathrm{i}(x,y,t)\frac{\partial \Delta z_\mathrm{i}(x,y,t)}{\partial t}. \tag{B12}$$

The entrainment flux of water

$$F^q_\mathrm{entrainment} \doteq -\bar{\rho}_\mathrm{i}(t)\frac{\mathrm{d}\bar{z}_\mathrm{i}(t)}{\mathrm{d}t} \tag{B13}$$

is associated with changes in mean inversion height. The term

$$F^q_{\text{fluctuations}} \doteq -\frac{1}{A}\iint_A \mathrm{d}x\,\mathrm{d}y\,\Delta\rho_{\mathrm{i}}(x,y,t)\frac{\partial \Delta z_{\mathrm{i}}(x,y,t)}{\partial t} \tag{B14}$$

is associated with fluctuations of the inversion height about its mean. The sign in the definition of $F^q_{\text{entrainment}}$ and $F^q_{\text{fluctuations}}$ is a matter of convention. Note that a temporally constant inversion height forces $F^q_{\text{entrainment}} = 0$ but not necessarily $F^q_{\text{fluctuations}} = 0$. Overall we can write

$$\frac{\mathrm{d}Q(t)}{\mathrm{d}t} = F^q_{\text{base}} - F^q_{\text{inv}} - F^q_{\text{entrainment}} - F^q_{\text{fluctuations}}. \tag{B15}$$

It remains to specify the meaning of F^q_{base} and F^q_{inv}. These are unrelated to changes in the location and shape of the inversion, which are represented by $F^q_{\text{entrainment}}$ and $F^q_{\text{fluctuations}}$. We hence account for surface precipitation ($F^q_{\text{precipitation}}$) and the surface moisture flux (F^q_{surface}), and for subsidence ($F^q_{\text{subsidence}}$), resolved scale dynamics (F^q_{resolved}), sub-grid scale dynamics ($F^q_{\text{unresolved}}$), and spurious mixing (F^q_{spurious}) at the inversion:

$$F^q_{\text{base}} \doteq F^q_{\text{precipitation}} + F^q_{\text{surface}} \tag{B16}$$

$$F^q_{\text{inv}} \doteq F^q_{\text{subsidence}} + F^q_{\text{resolved}} + F^q_{\text{unresolved}} + F^q_{\text{spurious}} \tag{B17}$$

The boundary layer water budget equation then reads

$$\begin{aligned}\frac{\mathrm{d}Q(t)}{\mathrm{d}t} = {} & F^q_{\text{precipitation}} + F^q_{\text{surface}} - F^q_{\text{entrainment}} \\ & - F^q_{\text{subsidence}} - F^q_{\text{fluctuations}} - F^q_{\text{resolved}} - F^q_{\text{unresolved}} - F^q_{\text{spurious}}.\end{aligned} \tag{B18}$$

We define F^q_{mixing}, the water flux across the inversion due resolved scale and sub-grid scale dynamics at the inversion, fluctuations in inversion height, and spurious mixing:

$$F^q_{\text{mixing}} = F^q_{\text{fluctuations}} + F^q_{\text{resolved}} + F^q_{\text{unresolved}} + F^q_{\text{spurious}} \tag{B19}$$

The boundary layer water budget equation then reads

$$\frac{\mathrm{d}Q(t)}{\mathrm{d}t} = F^q_{\text{precipitation}} + F^q_{\text{surface}} - F^q_{\text{entrainment}} - F^q_{\text{subsidence}} - F^q_{\text{mixing}}. \tag{B20}$$

Appendix C: Resolution

The dependence on resolution of boundary layer growth, entrainment, decoupling, LWP, and cloud radiative effect (CRE) in the course of a diurnal cycle at different wind speeds is documented here. The simulations $M^{-,0,+}_{\text{fine}}$ with double resolution in each dimension are compared with the simulations $M^{-,0,+}$ (Table 2). Figures C1 (time series) and C2, C3 (vertical profiles) show the results.

The high resolution simulations have systematically higher LWP values than the reference resolution simulations (Fig. C1a). This is a consequence of reduced mixing at the inversion at higher resolution (Sect. 2.1.2); the finding is supported by the cloud water profiles (Figs. C2a, b and C3a, b): lower resolution leads to a stronger reduction of cloud water in downdrafts compared to updrafts. The LWP response to wind speed and the evolution of LWP in the course of the diurnal cycle are robust against an increase in resolution. In particular, higher wind speed causes higher LWP values in the morning and a stronger LWP suppression later in the day at both resolutions, thereby expanding the morning–afternoon contrast and accentuating the LWP diurnal cycle (Sect. 3.1.3).

The high resolution simulations have a higher cloud fraction (Fig. C1b) due to reduced mixing and entrainment at the inversion at higher resolution. Owing to the systematically higher LWP values and higher cloud fraction, the high resolution simulations

have a stronger CRE (Fig. C1c). The CRE peaks shortly before noon at both resolutions with values that increase with wind speed, while afternoon CRE values become less dependent on wind speed owing to the wind speed-dependent daytime suppression of LWP (Sect. 3.1.3).

Boundary layer height (Fig. C1d) and entrainment rate (Fig. C1e) depend weakly on resolution, indicating that the model is robust in this respect against higher mixing and entrainment at the lower resolution. The higher resolution simulations produce, however, systematically higher decoupling (Fig. C1f). This higher decoupling has little effect on surface (10 m) wind speed (Fig. C1g), but increases surface layer temperature (Fig. C1h) and water vapor (Fig. C1i). Despite the higher surface layer temperature and moisture, the parameterizations of the surface sensible heat and moisture fluxes produce similar surface fluxes at the two resolutions (Fig. C1j and k).

Vertical total water profiles are shown in Figs. C2c and C3c. Reduced mixing and entrainment at the inversion increases total water content throughout the boundary layer, while higher decoupling at higher resolution increases total water near the surface (see also Fig. C1i). Profiles of ζ_{q_t} (Figs. C2d and C3d) reveal that at higher resolution, vertical moisture transport becomes less efficient only near the surface ($z/z_i = 0$ to $z/z_i \approx 0.1$). Concurrently, resolved scale vertical moisture tranport is faster at higher resolution throughout the boundary layer (Figs. C2e, f and C3e, f). We conclude that the cause of higher decoupling at higher resolution is a reduced efficiency of subgrid-scale vertical tranport (not shown), which dominates vertical transport near the surface.

We note that increased resolution has only a small effect on TKE production by buoyancy in the sub-cloud layer both during the nighttime period N (10:20–11:20 UT) (Fig. C2g) as well as in the afternoon (22:30–23:30 UT) (Fig. C3g). However, TKE production by shear strongly increases with resolution in the sub-cloud layer (Figs. C2h and C3h). Concurrently, TKE production by buoyancy is enhanced at cloud level at higher resolution (Figs. C2g and C3g). Stratification of TKE production by buoyancy by updrafts and downdrafts (Figs. C2i, j and C3i, j) reveals that the additional TKE production by buoyancy at cloud level originates from downdrafts. This is a consequence

of reduced mixing and entrainment at the inversion at higher resolution, which leads to reduced entrainment warming and drying of cloud level downdrafts. The effect also appears in the time series of TKE production by buoyancy, stratified by updrafts and downdrafts in the cloud- and sub-cloud layer (Fig. C2m–p): the time series of TKE production by buoyancy in cloud downdrafts (Fig. C2m) shows a systematic increase in response to higher resolution.

Acknowledgements. This work is supported by the U.S. Department of Energy (DOE) Atmospheric System Research Program grant DE-SC0006972, the U.S. National Oceanic and Atmospheric Administration (NOAA) Climate Program Office through the Climate Process Team, Cloud Macrophysical Parameterization and its Application to Aerosol Indirect Effects, and by NOAA's Climate Goal. Simulations were carried out on the NOAA Research and Development High Performance Computing System.

References

Bertin, X., Prouteau, E., and Letetrel, C.: A significant increase in wave height in the North Atlantic Ocean over the 20th century, Global Planet. Change, 106, 77–83, doi:10.1016/j.gloplacha.2013.03.009, 2013. 28399, 28420

Blossey, P. N., Bretherton, C. S., Zhang, M., Cheng, A., Endo, S., Heus, T., Liu, Y., Lock, A. P., Roode, S. R., and Xu, K.-M.: Marine low cloud sensitivity to an idealized climate change: the CGILS LES intercomparison, Journal of Advances in Modeling Earth Systems, 5, 234–258, doi:10.1002/jame.20025, 2013. 28397

Bony, S. and Dufresne, J.-L.: Marine boundary layer clouds at the heart of tropical cloud feedback uncertainties in climate models, Geophys. Res. Lett., 32, L20806, doi:10.1029/2005GL023851, 2005. 28397

Bretherton, C. S.: A conceptual model of the stratus-trade cumulus transition in the subtropical oceans, in: Proc. 11th Int. Conf. on Clouds and Precipitation, Vol. 1, Montreal, PQ, Canada, Int., comm. on Clouds and Precip., and Int. Assoc. Meteor. Atmos. Physics, 374–377, 1992. 28412, 28415

Bretherton, C. S. and Wyant, M. C.: Moisture transport, lower-tropospheric stability, and decoupling of cloud-topped boundary layers, J. Atmos. Sci., 54, 148–167, doi:10.1175/1520-0469(1997)054<0148:MTLTSA>2.0.CO;2, 1997. 28412, 28415

Bretherton, C. S., Blossey, P. N., and Jones, C. R.: Mechanisms of marine low cloud sensitivity to idealized climate perturbations: a single-LES exploration extending the CGILS cases, J. Adv. Mod. Earth Sys., 5, 316–337, doi:10.1002/jame.20019, 2013. 28398

Caldwell, P. and Bretherton, C. S.: Response of a subtropical stratocumulus-capped mixed layer to climate and aerosol changes, J. Climate, 22, 20–38, doi:10.1175/2008JCLI1967.1, 2009. 28397, 28398

Chen, Y.-C., Xue, L., Lebo, Z. J., Wang, H., Rasmussen, R. M., and Seinfeld, J. H.: A comprehensive numerical study of aerosol–cloud–precipitation interactions in marine stratocumulus, Atmos. Chem. Phys., 11, 9749–9769, doi:10.5194/acp-11-9749-2011, 2011. 28398

Clement, A. C., Burgman, R., and Norris, J. R.: Observational and model evidence for positive low-level cloud feedback, Science, 325, 460–464, doi:10.1126/science.1171255, 2009. 28397

Colón-Robles, M., Rauber, R. M., and Jensen, J. B.: Influence of low-level wind speed on droplet spectra near cloud base in trade wind cumulus, Geophys. Res. Lett., 33, L20814, doi:10.1029/2006GL027487, 2006. 28398

Dobrynin, M., Murawski, J., Baehr, J., and Ilyina, T.: Detection and attribution of climate change signal in ocean wind waves, J. Climate, 28, 1578–1591, doi:10.1175/JCLI-D-13-00664.1, 2015. 28399, 28420

Grell, G. A., Peckham, S. E., Schmitz, R., McKeen, S. A., Frost, G., Skamarock, W. C., and Eder, B.: Fully coupled "online" chemistry within WRF model, Atmos. Environ., 39, 6957–6975, doi:10.1016/j.atmosenv.2005.04.027, 2005. 28401

Hande, L. B., Siems, S. T., and Manton, M. J.: Observed trends in wind speed over the Southern Ocean, Geophys. Res. Lett., 39, L11802, doi:10.1029/2012GL051734, 2012. 28399, 28420

Hartmann, D. L. and Doelling, D.: On the net radiative effectiveness of clouds, J. Geophys. Res., 96, 869–891, doi:10.1029/90JD02065, 1991. 28397

Hartmann, D. L. and Short, D. A.: On the use of earth radiation budget statistics for studies of clouds and climate, J. Atmos. Sci., 37, 1233–1250, doi:10.1175/1520-0469(1980)037<1233:OTUOER>2.0.CO;2, 1980. 28397

Hartmann, D. L., Ockert-Bell, M. E., and Michelsen, M. L.: The effect of cloud type on earth's energy balance: global analysis, J. Climate, 5, 1281–1304, doi:10.1175/1520-0442(1992)005<1281:TEOCTO>2.0.CO;2, 1992. 28397

Hemer, M. A., Fan, Y., Mori, N., Semedo, A., and Wang, X. L.: Projected changes in wave climate from a multi-model ensemble, Nature Climate Change, 3, 471–476, doi:10.1038/nclimate1791, 2013. 28399, 28420

Jeuken, A. B. M., Siegmund, P. C., Heijboer, L. C., Feichter, J., and Bengtsson, L.: On the potential of assimilating meteorological analyses in a global climate model for the purpose of model validation, J. Geophys. Res., 101, 16939–16950, doi:10.1029/96JD01218, 1996. 28422

Katzwinkel, J., Siebert, H., and Shaw, R. A.: Observation of a self-limiting, shear-induced turbulent inversion layer above marine stratocumulus, Bound.-Lay. Meteorol., 145, 131–143, doi:10.1007/s10546-011-9683-4, 2012. 28401, 28416

Kazil, J., Wang, H., Feingold, G., Clarke, A. D., Snider, J. R., and Bandy, A. R.: Modeling chemical and aerosol processes in the transition from closed to open cells during VOCALS-REx, Atmos. Chem. Phys., 11, 7491–7514, doi:10.5194/acp-11-7491-2011, 2011. 28401

Kazil, J., Feingold, G., Wang, H., and Yamaguchi, T.: On the interaction between marine boundary layer cellular cloudiness and surface heat fluxes, Atmos. Chem. Phys., 14, 61–79, doi:10.5194/acp-14-61-2014, 2014. 28401

McInnes, K. L., Erwin, T. A., and Bathols, J. M.: Global climate model projected changes in 10 m wind speed and direction due to anthropogenic climate change, Atmos. Sci. Lett., 12, 325–333, doi:10.1002/asl.341, 2011. 28399, 28420

Meehl, G. A., Covey, C., Delworth, T., Latif, M., McAvaney, B., Mitchell, J. F. B., Stouffer, R. J., and Taylor, K. E.: The WCRP CMIP3 multimodel dataset: a new era in climate change research, B. Am. Meteorol. Soc., 88, 1383–1394, doi:10.1175/BAMS-88-9-1383, 2007. 28398

Mellado, J. P., Stevens, B., and Schmidt, H.: Wind shear and buoyancy reversal at the top of stratocumulus, J. Atmos. Sci., 71, 1040–1057, doi:10.1175/JAS-D-13-0189.1, 2014. 28401, 28416

Nuijens, L. and Stevens, B.: The influence of wind speed on shallow marine cumulus convection, J. Atmos. Sci., 69, 168–184, doi:10.1175/JAS-D-11-02.1, 2012. 28399

Petters, J. L.: The impact of radiative heating and cooling on marine stratocumulus dynamics, PhD thesis, The Pennsylvania State University, 2009. 28411

Schneider, S. H.: Cloudiness as a global climatic feedback mechanism: the effects on the radiation balance and surface temperature of variations in cloudiness, J. Atmos. Sci., 29, 1413–1422, doi:10.1175/1520-0469(1972)029<1413:CAAGCF>2.0.CO;2, 1972. 28397

Servain, J., Caniaux, G., Kouadio, Y. K., McPhaden, M. J., and Araujo, M.: Recent climatic trends in the tropical Atlantic, Clim. Dynam., 43, 3071–3089, doi:10.1007/s00382-014-2168-7, 2014. 28399, 28420

Skamarock, W. C., Klemp, J. B., Dudhia, J., Gill, D. O., Barker, D. M., Duda, M. G., Huang, X.-Y., Wang, W., and Powers, J. G.: A Description of the Advanced Research WRF Version 3, Tech. Rep. NCAR/TN-475+STR, National Center for Atmospheric Research, Boulder, CO, USA, 2008. 28401

Soden, B. J. and Vecchi, G. A.: The vertical distribution of cloud feedback in coupled ocean-atmosphere models, Geophys. Res. Lett., 38, L12704, doi:10.1029/2011GL047632, 2011. 28397

Stephens, G. L.: Cloud feedbacks in the climate system: a critical review, J. Climate, 18, 237–273, doi:10.1175/JCLI-3243.1, 2005. 28397

Stevens, B., Moeng, C.-H., Ackerman, A. S., Bretherton, C. S., Chlond, A., de Roode, S., Edwards, J., Golaz, J.-C., Jiang, H., Khairoutdinov, M., Kirkpatrick, M. P., Lewellen, D. C., Lock, A., Müller, F., Stevens, D. E., Whelan, E., and Zhu, P.: Evaluation of large-eddy simulations via observations of nocturnal marine stratocumulus, Mon. Weather Rev., 133, 1443–1462, doi:10.1175/MWR2930.1, 2005. 28400, 28402, 28405, 28407, 28423, 28441

Turton, J. D. and Nicholls, S.: A study of the diurnal variation of stratocumulus using a multiple mixed layer model, Q. J. Roy. Meteor. Soc., 113, 969–1009, doi:10.1002/qj.49711347712, 1987. 28411

Wang, S., Golaz, J.-C., and Wang, Q.: Effect of intense wind shear across the inversion on stratocumulus clouds, Geophys. Res. Lett., 35, L15814, doi:10.1029/2008GL033865, 2008. 28401, 28416

Wang, S., Zheng, X., and Jiang, Q.: Strongly sheared stratocumulus convection: an observationally based large-eddy simulation study, Atmos. Chem. Phys., 12, 5223–5235, doi:10.5194/acp-12-5223-2012, 2012. 28401, 28416

Webb, M. J., Senior, C. A., Sexton, D. M. H., Ingram, W. J., Williams, K. D., Ringer, M. A., McAvaney, B. J., Colman, R., Soden, B. J., Gudgel, R., Knutson, T., Emori, S., Ogura, T., Tsushima, Y., Andronova, N., Li, B., Musat, I., Bony, S., and Taylor, K. E.: On the contribution

of local feedback mechanisms to the range of climate sensitivity in two GCM ensembles, Clim. Dynam., 27, 17–38, doi:10.1007/s00382-006-0111-2, 2006. 28397

Williams, K. D. and Tselioudis, G.: GCM intercomparison of global cloud regimes: present-day evaluation and climate change response, Clim. Dynam., 29, 231–250, doi:10.1007/s00382-007-0232-2, 2007. 28397

Wood, R.: Stratocumulus Clouds, Mon. Weather Rev., 140, 2373–2423, doi:10.1175/MWR-D-11-00121.1, 2012. 28399, 28411

Wyant, M. C., Bretherton, C. S., Rand, H. A., and Stevens, D. E.: Numerical simulations and a conceptual model of the stratocumulus to trade cumulus transition, J. Atmos. Sci., 54, 168–192, doi:10.1175/1520-0469(1997)054<0168:NSAACM>2.0.CO;2, 1997. 28412, 28415

Wyant, M. C., Bretherton, C. S., Bacmeister, J. T., Kiehl, J. T., Held, I. M., Zhao, M., Klein, S. A., and Soden, B. J.: A comparison of low-latitude cloud properties and their response to climate change in three AGCMs sorted into regimes using mid-tropospheric vertical velocity, Clim. Dynam., 27, 261–279, doi:10.1007/s00382-006-0138-4, 2006. 28397

Xu, K.-M., Cheng, A., and Zhang, M.: Cloud-resolving simulation of low-cloud feedback to an increase in sea surface temperature, J. Atmos. Sci., 67, 730–748, doi:10.1175/2009JAS3239.1, 2010. 28397, 28398

Young, I. R., Zieger, S., and Babanin, A. V.: Global trends in wind speed and wave height, Science, 332, 451–455, doi:10.1126/science.1197219, 2011. 28399, 28400, 28420

Table 1. List of spin-up runs.

Spin-up	Domain size (km^2)	dt (s)	dx = dy (m)	dz (m)	Description
m	30 × 30	1.5	150	15	
m_{fine}	30 × 30	0.75	75	7.5	Fine resolution
l	60 × 60	1.5	150	15	
$l_{1:5}$	60 × 60	1.5	75	15	1 : 5 aspect ratio

Table 2. List of simulations. The superscripts −, 0, and + denote low, reference, and high geostrophic wind speed, respectively (see Sect. 2.2). All three superscripts are used when referring to all three simulations in a set. Simulations that use prescribed, spatially homogenized surface sensible heat and moisture fluxes carry an overbar.

Simulation	Spin-up	Domain size (km^2)	dt (s)	dx = dy (m)	dz (m)	Description
$M^{-,0,+}$	m	30 × 30	1.5	150	15	
$M^{-,0,+}_{\text{fine}}$	m_{fine}	30 × 30	0.75	75	7.5	Fine resolution
$M^{-,0,+}_{\text{dark}}$	m	30 × 30	1.5	150	15	Perpetual night
$L^{-,0,+}$	l	60 × 60	1.5	150	15	
$\bar{L}^{-,0,+}$	l	60 × 60	1.5	150	15	Surface heat fluxes from $L^{-,0,+}$
$\bar{L}^{-,0,+}_{\text{buoy}}$	l	60 × 60	1.5	150	15	Surface heat fluxes from $L^{-,0,+}$, no geostrophic wind

Table 3. Total (short-wave + longwave) cloud radiative effect ($W\,m^{-2}$) averaged over the 24 h duration of the simulations. Simulations are given in parentheses (Table 2).

Resolution	Low wind speed	Reference wind speed	High wind speed
$dx = dy = 150\,m$, $dz \approx 15\,m$, $dt = 1.5\,s$	−136.3 (M^-)	−141.0 (M^0)	−143.9 (M^+)
$dx = dy = 75\,m$, $dz \approx 7.5\,m$, $dt = 0.75\,s$	−148.2 (M^-_{fine})	−155.2 (M^0_{fine})	−157.7 (M^+_{fine})

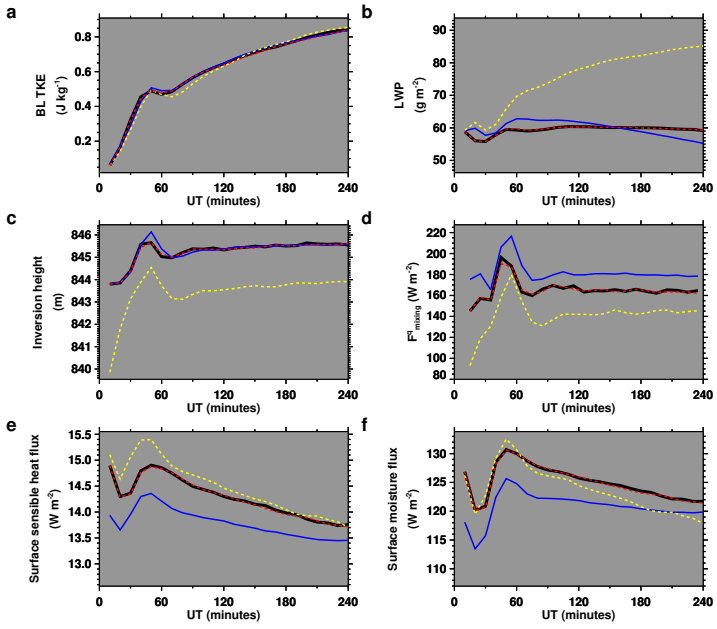

Figure 1. Time series from the spin-up runs m (black), m_{fine} (yellow), l (red), $l_{1:5}$ (blue). F^q_{mixing} is defined in Eq. (2). The spin-up runs are listed in Table 1.

please add uncertainty or std dev to observed values if possible.

Are the light gray shaded areas supposed to indicate this? If so, it is not clear from the caption.

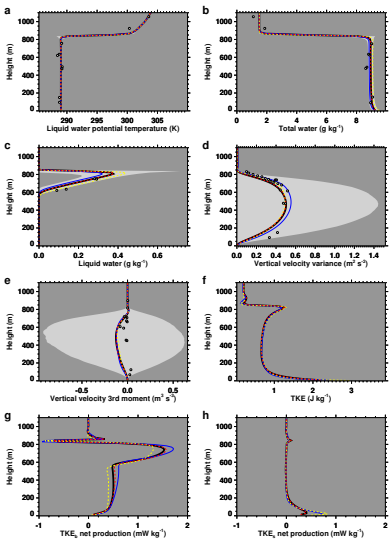

Figure 2. Final state of the spin-up runs (initial states of simulations). Mean final state (black) and values between the 10th and 90th percentiles (light gray, in plots with observations) of the spin-up run m, and the mean final state of the spin-up runs m_{fine} (yellow), l (red), $l_{1:5}$ (blue). DYCOMS II RF01 observations (Stevens et al., 2005) are represented by open circles. The spin-up runs are listed in Table 1. TKE_b denotes buoyant production, TKE_s shear production of turbulence kinetic energy.

28441

What time period do these cover?

Is the forcing steady in the spin up period?

why does the wind speed vary in the nocturnal case?

why aren't the initial values the same?

too many panels. are they all necessary?

4 per figure.

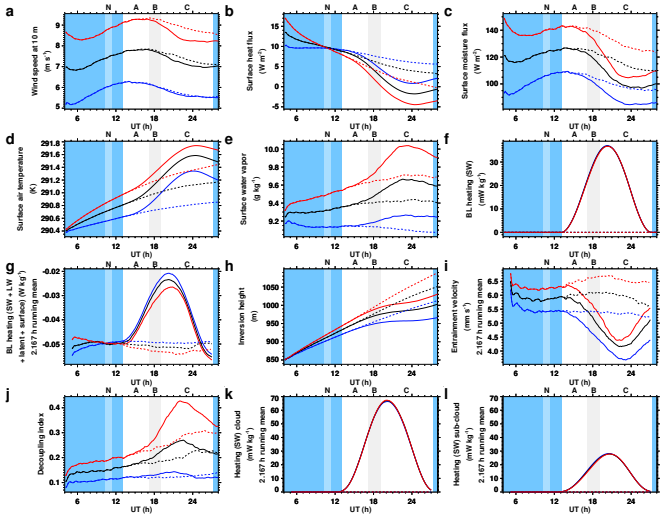

Figure 3. Wind speed and the diurnal cycle. Time series from simulations M^- (blue), M^0 (black), M^+ (red), solid curves, and from simulations M^-_{dark} (blue), M^0_{dark} (black), M^+_{dark} (red), dashed curves. A low-pass (running mean) filter was applied where indicated to reduce noise. Blue shading indicates nighttime.

what do N A B C indicate?
Please add this to caption.

28442

Discussion Paper | Discussion Paper | Discussion Paper | Discussion Paper |

too many panels. are they all necessary?

4 per figure.

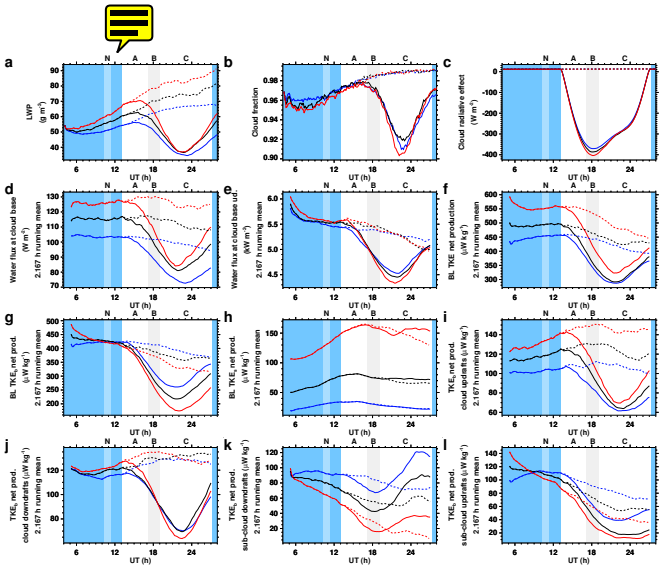

Figure 4. Wind speed and the diurnal cycle. Time series from simulations M^- (blue), M^0 (black), M^+ (red), solid curves, and from simulations M^-_{dark} (blue), M^0_{dark} (black), M^+_{dark} (red), dashed curves. A low-pass (running mean) filter was applied where indicated to reduce noise. Blue shading indicates nighttime. $\mathrm{TKE_b}$ denotes buoyant production, $\mathrm{TKE_s}$ shear production of turbulence kinetic energy. TKE production rates are given per total boundary layer air mass.

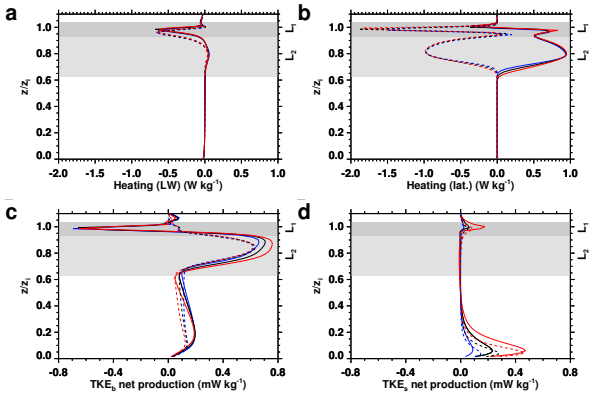

Figure 5. Long-wave heating **(a)**, latent heating **(b)**, and TKE net production from buoyancy **(c)** and shear **(d)**, averaged over the period N (10:20–11:20 UT) from the simulation M^- (blue), M^0 (black), M^+ (red). Solid curves denote values from updrafts, dashed curves values from downdrafts. Updraft and downdraft values are air mass weighted sums over the updraft or downdraft locations at each level, respectively, normalized by the level air mass. $\mathrm{TKE_b}$ denotes buoyant production, $\mathrm{TKE_s}$ shear production of turbulence kinetic energy.

too many panels. are they all necessary?

4 per figure.

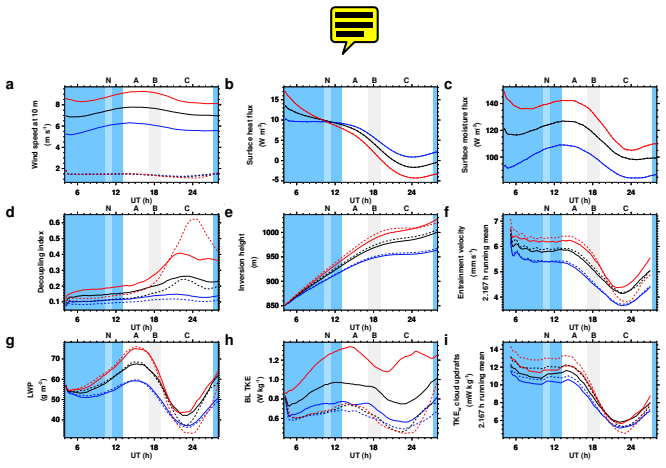

Figure 6. Buoyancy- and shear-driven dynamics. Time series from simulations $\bar{L}^-$ (blue), $\bar{L}^0$ (black), $\bar{L}^+$ (red), solid curves, and from simulations $\bar{L}^-_{buoy}$ (blue), $\bar{L}^0_{buoy}$ (black), $\bar{L}^+_{buoy}$ (red), dashed curves. A low-pass (running mean) filter was applied where indicated to reduce noise. Blue shading indicates nighttime. TKE and TKE_w are given per total boundary layer air mass, TKE_w denotes the vertical component of turbulence kinetic energy.

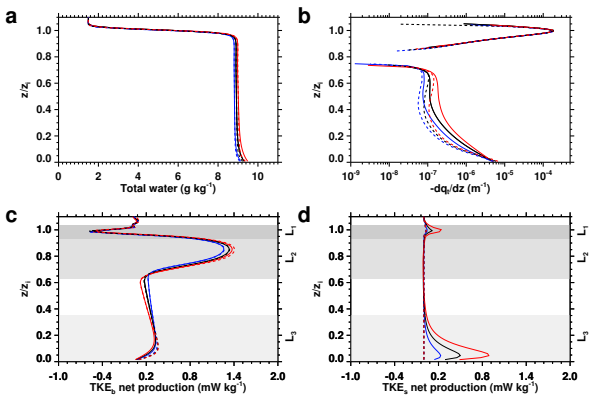

Figure 7. Buoyancy- and shear-driven dynamics. Profiles averaged over the period N (10:20–11:20 UT) from simulations L^- (blue), L^0 (black), L^+ (red), solid curves, and from simulations L^-_{buoy} (blue), L^0_{buoy} (black), L^+_{buoy} (red), dashed curves. TKE_b denotes buoyant production, TKE_s shear production of turbulence kinetic energy.

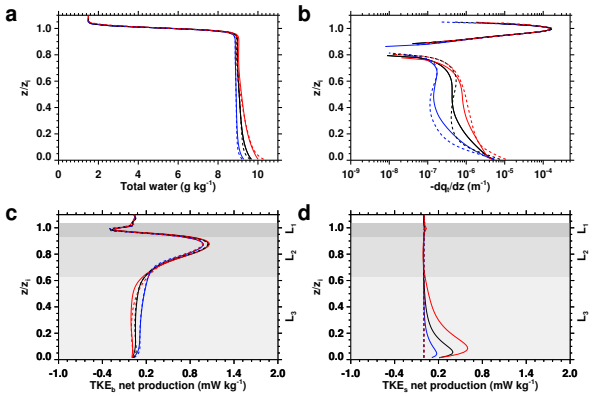

Figure 8. Buoyancy- and shear-driven dynamics. Profiles averaged over 1 h in the afternoon (22:30–23:30 UT) from simulations L^- (blue), L^0 (black), L^+ (red), solid curves, and from simulations L^-_{buoy} (blue), L^0_{buoy} (black), L^+_{buoy} (red), dashed curves. TKE_b denotes buoyant production, TKE_s shear production of turbulence kinetic energy.

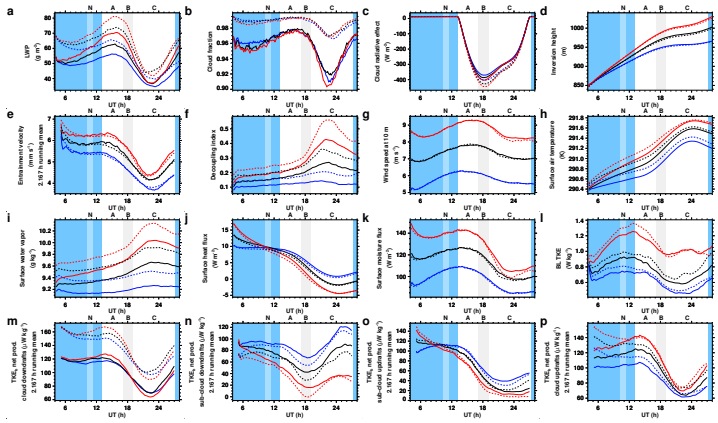

Figure C1. Effect of resolution. Solid curves denote simulations with the base resolution, dashed curves simulations with a doubled resolution in each dimension (Table 2). M^- (blue solid), M^0 (black solid), M^+ (red solid); M^-_{fine} (blue dashed), M^0_{fine} (black dashed), M^+_{fine} (red dashed). Blue shading indicates nighttime. TKE_b denotes buoyant production of turbulence kinetic energy. TKE production rates are given per total boundary layer air mass.

too many panels. are they all necessary?

4 per figure.

too many panels. are they all necessary?

4 per figure.

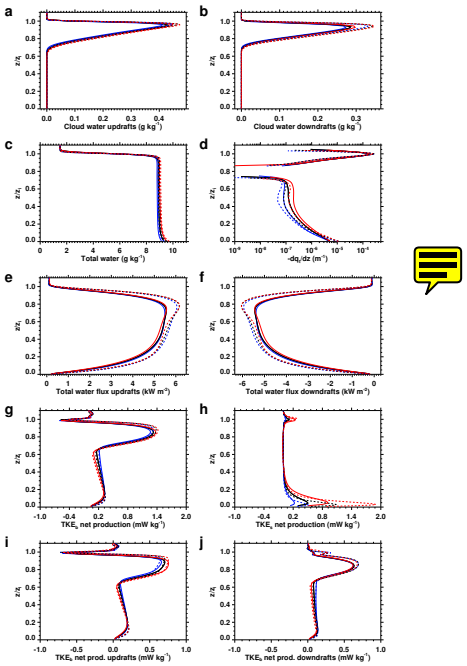

Figure C2. Effect of resolution. Profiles averaged over the period N (10:20–11:20 UT) from simulations M^- (blue), M^0 (black), M^+ (red), solid curves, and from simulations M^-_{fine} (blue), M^0_{fine} (black), M^+_{fine} (red), dashed curves. TKE_b denotes buoyant production, TKE_s shear production of turbulence kinetic energy. TKE_b and TKE_s in updrafts and downdrafts are air mass weighted sums over the updraft or downdraft locations at each level, respectively, normalized by the level air mass.

too many panels. are they all necessary?

4 per figure.

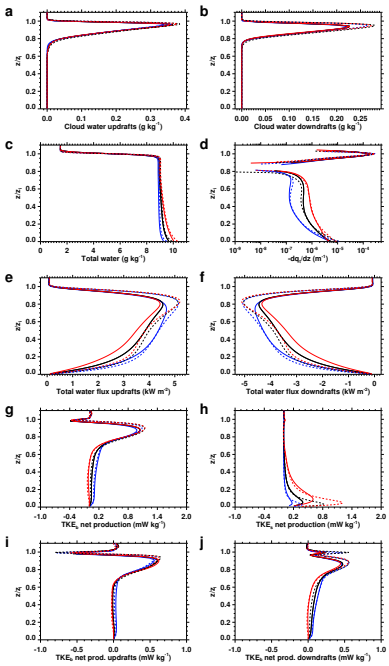

Figure C3. Effect of resolution. Profiles averaged over 1 h in the period C (22:30–23:30 UT) from simulations M^- (blue), M^0 (black), M^+ (red), solid curves, and from simulations M^-_{fine} (blue), M^0_{fine} (black), M^+_{fine} (red), dashed curves. $\mathrm{TKE_b}$ denotes buoyant production, $\mathrm{TKE_s}$ shear production of turbulence kinetic energy. $\mathrm{TKE_b}$ and $\mathrm{TKE_s}$ in updrafts and downdrafts are air mass weighted sums over the updraft or downdraft locations at each level, respectively, normalized by the level air mass.

Discussion Paper | Discussion Paper | Discussion Paper | Discussion Paper |